

Laser heating effect on Raman analysis of CO₂ co-existing as liquid and vapor in olivine-hosted melt inclusion bubbles

Charlotte L. DeVitre^{*α,β}, Kyle Dayton^α, Esteban Gazel^{† α}, Ayla Pamukçu^γ, Glenn Gaetani^δ, and Penny E. Wieser^β

^α Cornell University, Ithaca, NY 14850, USA.

^β Earth and Planetary Science, UC Berkeley, CA, USA.

^γ Earth and Planetary Sciences, Stanford University, Stanford, CA 94305, USA.

^δ Geology and Geophysics, Woods Hole Oceanographic Institution, Woods Hole, MA 02543, USA.

ABSTRACT

Raman spectroscopy has become the tool of choice for analyzing fluid inclusions and melt inclusion (MI) vapor bubbles as it allows the density of CO₂-rich fluids to be quantified. Measurements are often made at ambient temperature ($T_{\text{amb}} \sim 18\text{--}25^\circ\text{C}$), resulting in reported bulk densities between 0.2 and 0.7 g mL⁻¹ even though single-phase CO₂ is thermodynamically unstable under these conditions and instead consists of a liquid (~0.7 g mL⁻¹), and a vapor phase (~0.2 g mL⁻¹). Here, we present results from experiments conducted at T_{amb} and 37 °C (above the CO₂ critical temperature) on 14 natural CO₂-rich MI bubbles from Mount Morning, Antarctica. Here, we show that at T_{amb} , laser power strongly affects the CO₂ Raman spectrum of MI bubbles with bulk densities within the miscibility gap. High-power laser heating and low spectral resolution explain why published measurements have reported bulk densities within the miscibility gap at T_{amb} even when using an instrument-specific calibration.

KEYWORDS: Raman spectroscopy; Carbon dioxide; Fluid inclusions; Melt inclusions; Laser heating.

1 INTRODUCTION

Primary mineral-hosted fluid and melt inclusions are accidental μm -size droplets of fluids and melts, that get trapped in crystals during growth. Given that they are fully enclosed in crystals, these inclusions can act as time capsules and have long been used to investigate the physicochemical record of pressure (P), volume (Vol), temperature (T), and composition (X) conditions of geological processes, such as those associated with ore-deposit formation [e.g. Roedder 1979; 1984]. Melt inclusions are also of significant interest to igneous petrologists and volcanologists studying magma storage depths, because the host is thought to serve as a pressure vessel [Steele-Macinnis et al. 2011; Moore et al. 2015], and volatile solubility experiments in melts have resulted in geobarometers based on melt inclusion H₂O and CO₂ contents [e.g. Dixon 1997; Papale et al. 2006; Iacono-Marziano et al. 2012; Ghiorso and Gualda 2015; Allison et al. 2022].

Estimating volatile saturation pressures from melt inclusions requires accurate measurements of H₂O and CO₂. However, melt inclusions are composed of melt (quenched to a glass) \pm bubbles \pm crystals, so assessing melt inclusion volatile compositions requires measurements of volatiles in all existing phases. Recent work has shown that up to 90% of the CO₂ in a melt inclusion can be contained in vapor bubbles [e.g. Hartley et al. 2014; Moore et al. 2015; Wallace et al. 2015; Steele-MacInnis et al. 2017; Allison et al. 2021; Wieser et al. 2021], making it critical to quantify the CO₂ content of these bubbles. An increasingly popular approach to doing this involves estimating the CO₂ density of the bubble using Raman

spectroscopy, a non-destructive technique that provides high spatial resolution (~500 nm). The total CO₂ concentration in a melt-inclusion is determined through mass balance involving the CO₂ vapor density and the bubble volume and the concentration of CO₂ in the co-existing glass and the glass volume. This approach capitalizes on decades of research that has shown a relationship between the density of CO₂ and a spectral feature known as the CO₂ “Fermi diad” [Figure 1A; Gordon and McCubbin 1966]—two peaks located at ~1285.4 cm⁻¹ and ~1388.2 cm⁻¹ (hereby respectively named ν^- and ν^+) in a Raman spectrum. The distance between these peaks (ΔCO_2) is a function of CO₂ density, and this relation combined with the PVT properties of CO₂ from an Equation of State (EOS) is the basis to calibrate CO₂ densimeters [Rosso and Bodnar 1995; Kawakami et al. 2003; Yamamoto and Kagi 2006; Song et al. 2009; Fall et al. 2011; Wang et al. 2011; Lamadrid et al. 2017; Sublett et al. 2020; DeVitre et al. 2021].

Melt inclusions can be entrapped at variable depths that are frequently greater than 100 MPa, and the pressure inside a vapor bubble that forms at these entrapment depths will be similarly high. During storage, ascent, and syn-eruptive quenching, a melt inclusion can be subject to several processes, such as differential cooling and contraction of the olivine host and melt, post-entrapment crystallization, and H₂O loss through H⁺ diffusion, that reduce the volume of melt, and in turn pressure, in the inclusion. This pressure drop can result in the formation of the vapor bubble, which will be filled with volatiles if their solubility limits are reached. Given the lower solubility of CO₂ over H₂O in magmas, the vapor bubble is expected to be CO₂-rich. However, the amount of CO₂ that diffuses into the bubble during quenching is rate-limited, and the final

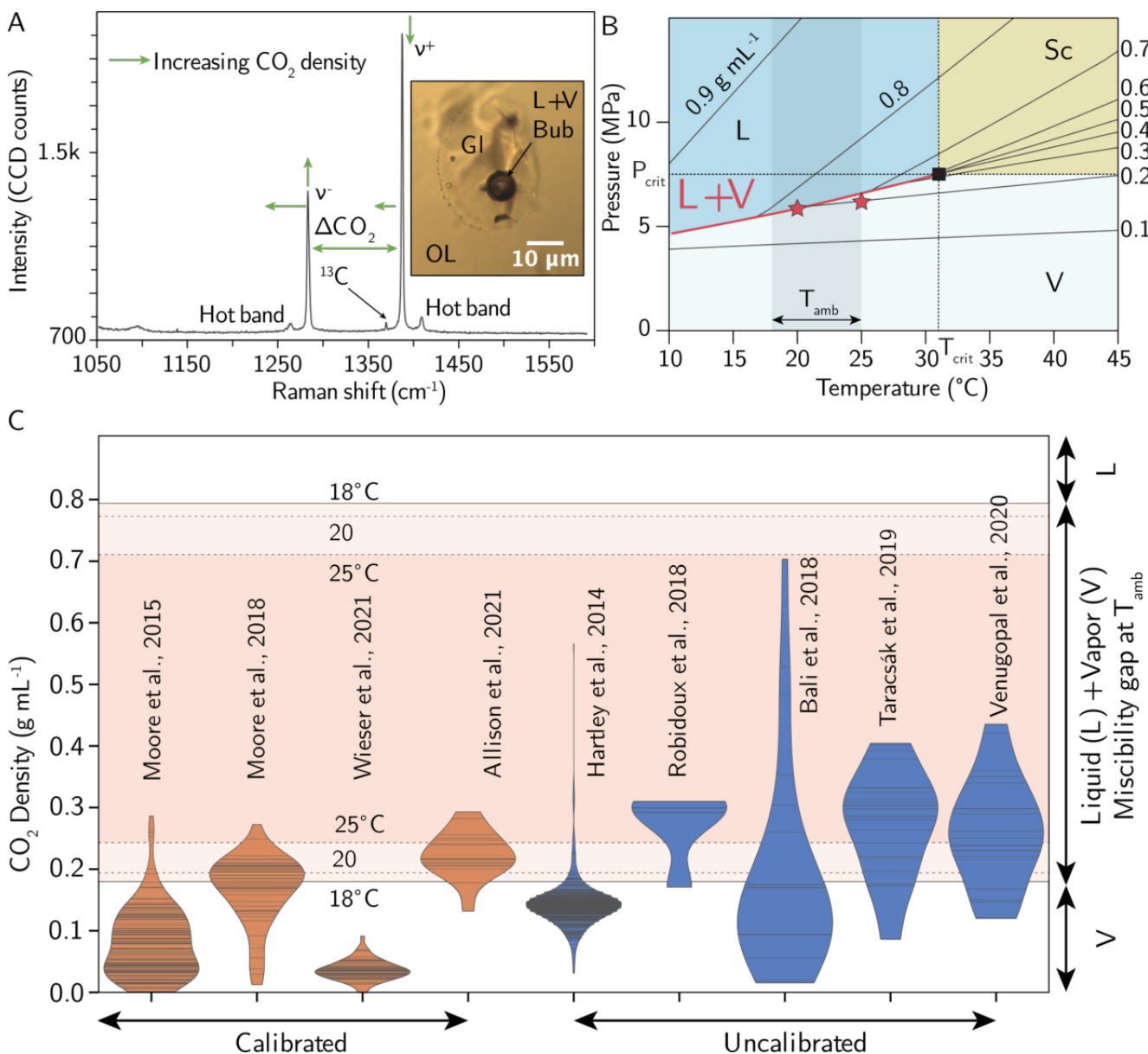


Figure 1: [A] Raman spectrum of a Mount Morning MI vapor bubble measured at 37 °C illustrating the CO₂ Fermi diad, hot bands, and ¹³C peaks. The effect of increasing CO₂ density is shown by the green arrows [B] Phase diagram of CO₂. L for liquid, V for vapor, Sc for Supercritical. The black lines are isochores, calculated using the EOS of Span and Wagner [1996]. The stars mark the isochoric path of pure CO₂ with a bulk density of 0.2 g mL⁻¹ at 20 °C and 25 °C. A bubble of this bulk density would be pure vapor at 25 °C but L+V at 20 °C. [C] CO₂ densities of vapor bubbles in natural melt inclusions measured at T_{amb} by Raman spectroscopy as reported in several literature articles. Note that many of these have measured and reported densities the miscibility gap at T_{amb} regardless of whether the instrument was specifically calibrated or not. Data reported from uncalibrated instruments generally report higher densities.

pressure of CO₂ in the bubble at ambient temperatures (T_{amb} , ~18–25 °C) is typically no more than 10s of MPa.

The CO₂ phase diagram shows that the CO₂ critical temperature (T_{crit}) is 31.1 °C at a pressure of 7.38 MPa, above which CO₂ is stable as a single supercritical phase (Figure 1B; isochores calculated using the EOS of Span and Wagner [1996] implemented in the NIST webbook*). At ambient temperatures (~18–25 °C), there is a miscibility gap (Figure 2B, C) across which two phases (liquid and vapor) co-exist. For ex-

ample, at 20 °C, a bubble with a CO₂ density <0.2 g mL⁻¹ ($\Delta CO_2 \lesssim 103.4$ cm⁻¹ on the Cornell Alpha 300R Raman instrument) will exist as a vapor phase, while a bubble with a density >0.7 g mL⁻¹ will exist as a liquid phase ($\Delta CO_2 \gtrsim 104.4$ cm⁻¹ on the Cornell instrument). A bubble with a bulk CO₂ density between these values (~0.2–0.7 g mL⁻¹) will be within the miscibility gap and consist of an outer liquid phase with a density of ~0.7 g mL⁻¹ and an inner vapor phase with a density of ~0.2 g mL⁻¹ [Roedder 1965; Roedder and Bodnar 1980; Wieser et al. 2021].

* <https://webbook.nist.gov/chemistry/fluid/>

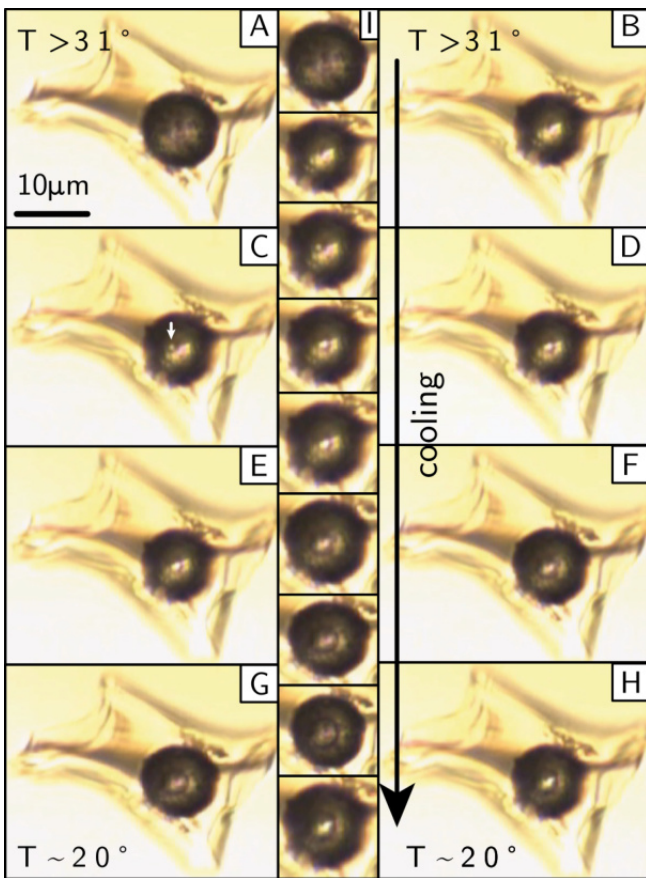


Figure 2: Fast-cooling experiment video stills of a Mount Morning MI bubble with a bulk CO_2 density of 0.54 g mL^{-1} (VB0.54). The sample is sitting on a Peltier thermoelectric module. [A–B] The temperature at the beginning of the experiment is above 31°C (T_{crit}), the two panels are stills at slightly different focus. The Peltier's connection polarity was flipped, and cooling begins. [C] Nucleation of a small vapor bubble is observed and indicated by the white arrow. [D–H] Cooling continues. [I] Bubble only panels in the middle show the nucleation of the vapor bubble inside the liquid from $T > T_{\text{crit}}$ to T_{amb} . Two videos are provided in the supporting information, one of this cooling experiment and another of a bubble at T_{amb} under microscope light where the vapor bubble can be seen bouncing in the liquid.

Consequently, analyses of fluid inclusions or melt inclusion vapor bubbles conducted at T_{amb} are expected to measure the density of either liquid or vapor CO_2 but no densities in between, even if the bulk density lies in this range. This is the case for measurements conducted in calibration apparatuses [Kawakami et al. 2003; Lin et al. 2007; Fall et al. 2011; Wang et al. 2011; DeVitre et al. 2021] and using certain synthetic fluid inclusions [Fall et al. 2011]. However, several studies of natural samples report densities measured at T_{amb} that span the miscibility gap [Figure 1C; e.g. Hartley et al. 2014; Moore et al. 2015; Bali et al. 2018; Moore et al. 2018; Robidoux et al. 2018; Taracsák et al. 2019; Venugopal et al. 2020; Allison et al. 2021]. Interestingly, the measurement at T_{amb} ($\sim 18\text{--}25^\circ\text{C}$) of natural samples with bulk densities in the miscibility gap has not been discussed heretofore.

Table 1: List of vapor bubbles analyzed in this study.

Sample name (MI)	Vapor bubble code	Bulk density at 37°C	Bubble radius (μm)
G170-002a_1_1	VB0.31	0.31	6.6
G170-002a_1_1	VB0.23	0.23	5.5
G170-002a_1_1	VB0.32	0.32	4.5
G170-002a_2_1	VB0.55	0.55	6.3
G170-002a_2_2	VB0.54	0.54	5.5
G170-004_1_1	VB0.53	0.53	9.1
G170-004_2_2	VB0.27	0.27	5.2
G170-004_2_2	VB0.35	0.35	4.4
G170-004_2_4	VB0.51	0.51	3.6
G170-004_2_5	VB0.40	0.40	3.7
G170-004_2_6	VB0.22	0.22	18.3
G170-004_2_8	VB0.39	0.39	8.6
G170-004_1_4	VB0.63	0.63	4.3
G170-004_2_1	VB0.28	0.28	7.4

Some of these results could be explained by the lack of an instrument specific calibration (Figure 1C). For example, the studies by Kawakami et al. [2003] or Yamamoto and Kagi [2006] can misestimate the density by up to $0.1\text{--}0.15 \text{ g mL}^{-1}$ [see Fig. 11 in DeVitre et al. 2021] if the calibration curve is not adjusted for the specific instrument being used. Such an overestimate corresponds to 40–60 % systematic offset on the measured bulk density for a 0.25 g mL^{-1} bubble and 17–25 % for a 0.60 g mL^{-1} bubble. This could be enough to explain some of the bulk densities in the miscibility gap that were measured at ambient temperatures without an instrument-specific calibration. Nevertheless, this is still insufficient to explain published bulk densities above $>0.35 \text{ g mL}^{-1}$ [e.g. Moore et al. 2015; Bali et al. 2018; Moore et al. 2018; Allison et al. 2021] regardless of whether they were calibrated. In this case, one potential explanation for these seemingly “impossible” results is that laser heating during analysis increases the temperature in the bubble above T_{crit} . Fall et al. [2011] suggested that significant laser heating (more than tenths of a degree) should not occur during analysis with an estimated laser power at sample of $\sim 10 \text{ mW}$ or less. Nevertheless, a more recent study of laser heating in CO_2 rich, high-density fluid inclusions ($>0.68 \text{ g mL}^{-1}$) implies that at laser powers $\geq 10 \text{ mW}$, tens to hundreds of degrees of laser-induced heating could occur. Furthermore, the extent of such heating depends mainly on the absorption coefficient of the host mineral, where quartz \ll olivine $<$ opx \approx cpx \ll spinel [Hagiwara et al. 2021].

Aiming to provide researchers with better understanding and protocols to accurately measure MI bubble CO_2 densities, particularly for those with bulk densities in the miscibility gap at T_{amb} , we explore the heating effects of the laser beam in more detail. Here, we present the results of a series of Raman measurements at different laser powers, diffraction gratings, temperatures, and integration times conducted on natural CO_2 -rich vapor bubbles in olivine-hosted melt inclusions from Mount Morning, Antarctica. Using standard analytical and data reduction procedures at 24°C , all the samples ex-

cept for two yield calculated CO₂ densities within the miscibility gap. We show that laser heating to near or above T_{crit} can occur in analyses conducted at high laser power, and it is possible to discern and resolve the contribution of both liquid and vapor phase vibrations to the Raman spectrum in analyses conducted at low laser power. Increasing laser power causes the liquid and vapor peaks of CO₂ to converge until they are indistinguishable, and a single peak model fit to each CO₂ band results in a calculated density in the miscibility gap. For measurements conducted above the T_{crit} we show that high laser power may cause further heating of the sample, which in turn decreases the measured Fermi separation and can lead to underestimation of the CO₂ density. In this contribution, we use the term “band” when referring to a region of the CO₂ Fermi diad which may encompass more than one peak (i.e. we may refer to v^+ or v^- bands where both a liquid peak and vapor peak may contribute to each) and we use peak when referring to a single relatively symmetric peak.

2 MATERIALS AND METHODS

2.1 Samples

We analyzed 14 vapor bubbles contained in 11 olivine-hosted melt inclusions (two melt inclusions hosted multiple bubbles). The vapor bubbles had radii of 3.5–9 μm , except for one bubble with a radius of 18 μm (Table 1). Crystals were mounted in a 1-inch epoxy mount, which we ground to 1.5 mm thickness and polished so that the melt inclusions were within ~5–30 μm of the surface for high-precision Raman analysis. A final ~0.3 μm alumina powder polish was used to ensure best visibility. We refer to vapor bubbles in this study only by the name they were assigned according to their bulk density measured at 37 °C (Vapor bubble name; Table 1). For example, VB0.63 has a measured bulk density of 0.63 g mL⁻¹ and is enclosed in melt inclusion G170-004_1_4. Liquid and vapor phases were evident under LED microscope in all vapor bubbles at 24 °C (Figure 2), except for six with measured densities at 24 °C of either pure vapor (VB0.22, VB0.23; Table 1) or near that of pure vapor (VB0.31, VB0.32, VB0.28, VB0.35).

2.2 Raman spectroscopy for MI bubble CO₂

We collected Raman spectra using a WiTec Alpha 300R Raman spectrometer at the Department of Earth and Atmospheric Sciences at Cornell University, using a green solid state 532.077 nm laser focused as an excitation source with a 50× objective (x0.55NA, 9.1 mm focal distance). Our instrument at Cornell University is equipped with a TruePower system for determining the laser power in the optical fiber, which allows for adjustments with an accuracy of <0.1 mW. To assess uncertainty, repeated measurements of two bubbles were collected at the Department of Earth and Planetary Sciences at the University of California, Berkeley using a nearly identical WiTec Alpha 300R Raman (see [Supplementary Material](#) for details). The Cornell instrument was calibrated using the FDCA and method described in [DeVitre et al. 2021] to obtain new calibration equations relating CO₂ density and ΔCO_2 . These equations are of the same form but slightly offset from those reported by DeVitre et al. [2021], which were calibrated

for a different Witec Alpha 300R Raman instrument at the Cornell Center for Materials Research. Spectra were initially collected for all 14 vapor bubbles at both 24 °C and 37 °C with five accumulations of 45 s of integration time (total analytical time = 225 second) in a single window using 1800 grooves/mm (~0.54 cm⁻¹ spectral resolution) and 12 mW laser power.

Three of the measured bubbles (VB0.63, VB0.51 and VB0.28; Figure 3) were selected for additional analysis as their calculated densities (see [Section 2.3](#)) are within the miscibility gap at 24 °C (0.28, 0.51, and 0.63 g mL⁻¹). Each of these bubbles was measured with at least 7 different laser powers (0.5, 1, 2, 5, 8, 12, and 20 mW) with the analytical settings described above at both 24 °C and 37 °C. Note that laser powers of 8–12 mW are the most frequently used in this type of analyses. Two of the bubbles were also analyzed using the 2400 grooves/mm diffraction grating (~0.31 cm⁻¹ spectral resolution) at 24 °C. Finally, one of the bubbles was analyzed at 5 and 10 mW with different integration times (5, 10, 20, 30, 45, 90, and 200 s) and number of accumulations (1 to 5). A total of 117 spectra were acquired, 81 at 24 °C and 36 at 37 °C.

Neon (Ne) spectra were collected immediately before and after each CO₂ analysis using the same grating as the unknown and three accumulations of 45 s integration time, to correct for non-linearity of the Raman shift axis [Lin et al. 2007; Wang et al. 2011; Lamadrid et al. 2017; DeVitre et al. 2021]. For all experiments, the temperature was regulated using a set-up that included a Peltier thermoelectric stage with a center hole and an Omega UTC–USB type K thermocouple for temperature monitoring on the surface of the epoxy mount.

2.3 Spectral post-processing and density calculation

Spectra were first baseline-subtracted using two-anchor point (~1200 cm⁻¹ and ~1450 cm⁻¹) linear subtraction on [Fityk](#) Open-Source Software [Wojdyr 2010]. We fit a Voigt peak (mixed Gaussian and Lorentzian model) on each main CO₂ peak (1285 cm⁻¹ and 1389 cm⁻¹). We selected Voigtian profiles given that for symmetric Raman peaks (like for single-phase CO₂ peaks), Voigt and Pseudo-Voigt functional forms are generally considered the most appropriate functional fitting forms [Yuan and Mayanovic 2017]. When hot bands (1270 cm⁻¹ and 1410 cm⁻¹) and ¹³C (1370 cm⁻¹) peaks were visible and overlapped with the main CO₂ peaks, we fit additional Voigt peaks to the spectra at those positions to reduce the effect of their residuals on the fitting of the main CO₂ peaks. In a separate exercise, we fit two peaks to each of the two main CO₂ peaks if liquid and vapor peaks were observed, and we also tested double-peak fits where only a single peak was evident. Finally, we peak-fit the same spectra using Python tool [DiadFit](#) v0.0.57 [Wieser and DeVitre 2023] to test sensitivity to peak-fitting method. With [DiadFit](#), we used a linear baseline subtraction anchored with two regions of spectrum near the [Fityk](#) anchor points and fit a single Voigt peak to each of the CO₂ peaks ([Supplementary Material](#) Fig. S1). As with [Fityk](#), we fit additional peaks when hot bands (1270 cm⁻¹ and 1410 cm⁻¹) and ¹³C (1370 cm⁻¹) were visible on the spectrum. We found no significant difference between the two peak-fitting methods ([Supplementary Material](#) Fig. S1). Following the methods described in [Lamadrid et



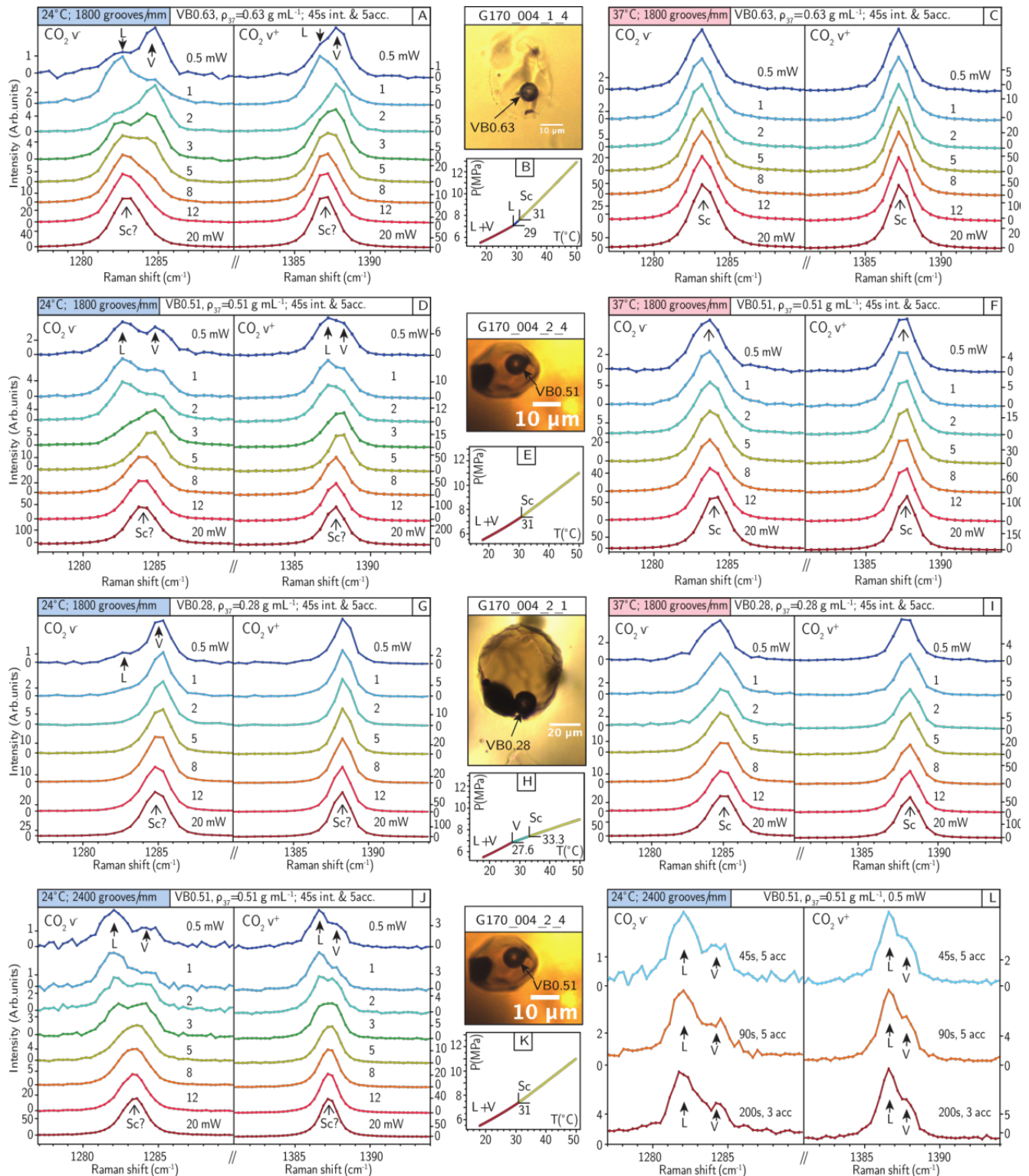


Figure 3: Closeup spectra of the lower (v^-) and upper (v^+) bands of CO_2 for vapor bubbles [A–C] VB0.63, VB0.51 (D–F at 1800 grooves/mm and J–L at 2400 grooves/mm) and [G–I] VB0.28. Panels on the left and at the very bottom show spectra measured at 24 °C [A, D, G, J, L] using different laser powers from 0.5 to 20 mW on each MI but constant integration time and accumulation number (45 s \times 5). Panels in the middle [B, E, H, K] show a photo micrograph of the MI in which each vapor bubble is contained along with an isochoric PT path for each bubble [B, E, H, K] calculated through the EOS of Span and Wagner [1996] assuming the bubbles are pure CO_2 . Panels on the right [C, F, I] show spectra measured at the same laser powers but while heating at 37 °C. Note that the peaks corresponding to L and V vibrations are discernible at low laser power but converge at higher power for all inclusions. Spectra at 37 °C are clearly single-phase spectra with a symmetric shape.

al. 2017], we corrected our data using two known Ne emission lines (1115.9919 cm⁻¹ and 1446.4696 cm⁻¹) that encompass the Fermi diad. We fit a single Voigt peak at 1446–1453 cm⁻¹ for the upper line and two Voigt peaks (1113–1120 cm⁻¹ and 1115–1122 cm⁻¹) for the lower line; the latter emission line appears as a double-peak on the Raman spectrum at the resolution of our grating. We then calculate the $\Delta\text{CO}_2\text{corr}$:

$$\Delta\text{CO}_2\text{corr} = \left(\frac{\Delta\text{Ne}_{\text{known}}}{\Delta\text{Ne}_{\text{observed}}} \right) \times \Delta\text{CO}_2\text{uncorr} \quad (1)$$

where $\Delta\text{CO}_2\text{corr}$ is the corrected separation of the Fermi diad, $\Delta\text{Ne}_{\text{known}}$ is the expected separation of the Ne emission lines in air, $\Delta\text{Ne}_{\text{observed}}$ is the separation of the same Ne emission lines measured from each Raman spectrum and $\Delta\text{CO}_2 - \text{uncorr}$ is the measured separation of the Fermi diad.

Finally, we used the mid-density equation (0.13–0.70 g mL⁻¹ at 37 °C) obtained following the method of DeVitre et al. [2021] to determine the bubble CO₂ densities of each MI bubble at 37 °C:

$$\begin{aligned} \rho_{\text{CO}_2} = & -47.2609 + 0.4596005 \times \Delta\text{CO}_2\text{corr} \\ & + 0.0374189 \times (\Delta\text{CO}_2\text{corr} - 103.733)^2 \\ & - 0.0187173 \times (\Delta\text{CO}_2\text{corr} - 103.733)^3 \end{aligned} \quad (2)$$

where ρ_{CO_2} is the calculated density of the MI bubble. Note that Equation 2 is only calibrated for densities comprised between 0.13 and 0.70 g mL⁻¹ at 37 °C and should not be used to report densities measured under any other conditions.

3 RESULTS

In this section, we focus on the results for the three vapor bubbles (VB0.63, VB0.51, VB0.28) that were selected for in-depth experiments.

3.1 Peak Fitting

As the density of CO₂ increases, both the v^- and v^+ peaks move to lower wavenumbers although v^- moves the most (Figure 1A). In cases where two peaks are observed near the v^- and v^+ positions, the higher wavenumber peak at either position is from the vapor and the lower wavenumber peak is from the liquid. When we fit two peaks to each CO₂ diad band in spectra that display either a clear contribution of two peaks or there is noticeable broadness and asymmetry to the peak, the resulting $\Delta\text{CO}_2\text{corr}$ (Figure 4) correspond well to those expected for vapor CO₂ (~103.35 cm⁻¹) and liquid CO₂ (~104.45 cm⁻¹) on our instrument at 24 °C. In these cases, when a single peak is fit to the CO₂ band, the residuals from the peak corresponding to the second phase can significantly affect fitting, and the resulting peak position lies somewhere between the peak positions of each phase (Figure 4). Fitting 2 peaks when only one is discernible yields two $\Delta\text{CO}_2\text{corr}$ that are nearly identical to each other (Figure 4; >12 mW).

3.2 3.2 VB0.63 ($\rho_{\text{CO}_2} = 0.63 \text{ g mL}^{-1}$)

At 24 °C, both liquid and vapor were identified microscopically and spectroscopically in VB0.63 (Figure 3A–C), and analyses at 37 °C yielded a CO₂ density of 0.63 g mL⁻¹. Based

on the isochoric path of a pure CO₂ fluid as calculated by the EOS of Span and Wagner [1996], a bubble of this density should turn to a liquid at ~29 °C and subsequently a supercritical phase above 31 °C (Figure 3B). For this bubble, separate peaks for liquid and vapor are well-resolved in spectra collected with the 1800 grooves/mm grating (Figure 3A) at laser powers of up to 2 mW, and the peaks are noticeably asymmetric up to 12 mW. The relative intensity of the liquid and vapor peaks varies slightly between the 0.5, 1, and 2 mW analyses. This is likely due to slight differences in fine focus or Brownian motion of the small vapor phase in the bubble (~3.5 μm diameter) during analysis, which results in analyzing variable amounts of liquid or vapor. Spectra from the 1800 grooves/mm grating at 8–12 mW laser power analyses show a broadness and asymmetry to the v^- peak, but it is challenging to visually discern a contribution of more than one phase to the spectrum. However, in spectra collected with the 2400 grooves/mm diffraction grating (Supplementary Material Figure S3), liquid and vapor contributions to the spectra are visually discernible at 8 and 10 mW. They are nearly indiscernible at 12 mW, but all peaks are noticeably asymmetric (see Supplementary Material for further discussion). Overall, it is challenging to visually discern the contribution of the two peaks in spectra acquired with the lower spectral resolution (~0.5–1 cm⁻¹) and higher laser powers (>5 mW) that are commonly used for melt inclusion vapor bubble measurements.

A single peak ($v_{1\text{pk}}$) fit by least squares minimization to the 8 mW, 1800 grooves/mm analysis (Figure 5A) does not match the center position or shape of the vapor bubble spectrum (particularly the v^- band) as closely as a double peak model ($v_{2\text{pk}}$) that accounts for the possible presence of a vapor phase in the bubble (Figure 5B–C). For comparison, Figure 5D–F shows the results of both models applied to the same spectrum acquired at 37 °C (when all CO₂ is found as a supercritical phase). Note that in this case, there is no physical reason for fitting more than one peak and using a $v_{2\text{pk}}$ model instead of $v_{1\text{pk}}$ model does not change the center position or significantly improve the fits. Further, the resulting relative intensities of the fitted positions for expected liquid and vapor are incoherent when comparing v^- to v^+ . For example, in Figure 5F, the lowest wavenumber (i.e. liquid) peak has the highest intensity for v^- but the lowest intensity for v^+ .

As laser power increases (3–12 mW at 1800 grooves/mm; 8–12 mW at 2400 grooves/mm) the intensity of the vapor phase peak decreases relative to that of the liquid phase peak, and at 20 mW (1800 grooves/mm) the vapor contribution appears to be completely gone (Figure 3A, C, Supplementary Material Figure S3). It is difficult to assess whether at 20 mW all the CO₂ has become supercritical (implying $T \geq T_{\text{crit}}$) or whether it has remained a liquid (29 °C < $T < T_{\text{crit}}$). However, the $\Delta\text{CO}_2\text{corr}$ from 20 mW/24 °C is very close to the one measured at 12 mW/37 °C. This could indicate the bubbles were at similar temperatures and are both a supercritical phase (Figure 6A). Additionally, at 20 mW and 37 °C, $\Delta\text{CO}_2\text{corr}$ is lower than at 24 °C, consistent with studies that measure decreasing $\Delta\text{CO}_2\text{corr}$ with increasing temperature for the same density of CO₂ [Fall et al. 2011; Wang et al. 2011; Sublett et al. 2020; DeVitre et al. 2021]. This could indicate that the CO₂ in

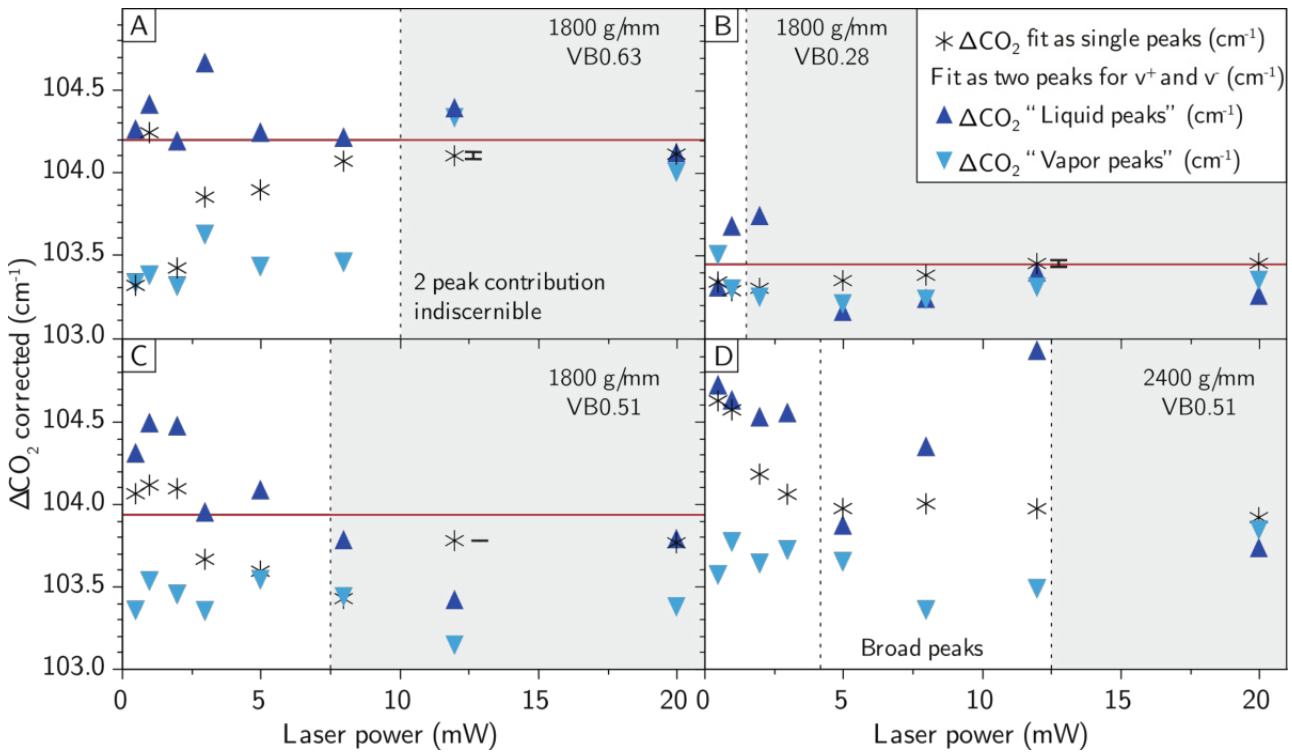


Figure 4: Laser power vs the corrected measured $\Delta\text{CO}_2\text{corr}$ for all three vapor bubbles collected with 45 s integration time and 5 accumulations. The black asterisks indicate $\Delta\text{CO}_2\text{corr}$ calculated by fitting a single peak model to each spectrum (Figure 6A; one peak per CO_2 band, a common way of fitting spectra). The triangles indicate the $\Delta\text{CO}_2\text{corr}$ measured by fitting a double-peak model to each spectrum (Figure 6C, acknowledging the contribution of both a vapor and liquid vibration in the spectrum). The upright dark blue triangles are $\Delta\text{CO}_2\text{corr}$ calculated using the two lowest wavenumber peaks (which should correspond to liquid vibration), and the downward light blue triangles are calculated using the two highest wavenumber peaks (which should be vapor vibration). Note that both models were fit regardless of whether one or two-phases were effectively resolved in the spectrum. The grey boxes indicate regions for which vapor and liquid contributions to the spectra were not clearly resolved. Red lines indicate the accepted $\Delta\text{CO}_2\text{corr}$ of our vapor bubbles when measured at 37 °C and using the best-fit intercept on Figure 6. Error bars on single peak-fits for this plot are the size of the symbols or smaller, for clarity only shown as an example on the 12 mW measurements (see Supplementary Material Fig. S1). [A] Bubble VB0.63 (0.63 g mL⁻¹) at 1800 grooves/mm. At low laser powers (<5 mW), the single peak model is alternatively skewed to either pure liquid or pure vapor due to the relative intensities of each peak in the spectrum (Figure 3A). For laser powers up to 10 mW, the single peak model predicts $\Delta\text{CO}_2\text{corr}$ somewhere in between the liquid and vapor $\Delta\text{CO}_2\text{corr}$. Above 12 mW, liquid and vapor peaks are clearly no longer resolved. [B] Bubble VB0.28 (0.28 g mL⁻¹) at 1800 grooves/mm. At most laser powers, L and V $\Delta\text{CO}_2\text{corr}$ are not simultaneously resolved. The fits at low laser power are heavily skewed to vapor, due to the overwhelming predominance of the vapor phase peak compared to the liquid phase peak as can be observed in Figure 3G. [C–D] Bubble VB0.51 (0.51 g mL⁻¹) at 1800 grooves/mm and at 2400 grooves/mm. Note that the $\Delta\text{CO}_2\text{corr}$ measured at 2400 grooves/mm are naturally higher by ~0.15 cm⁻¹ [a similar effect of gratings is shown in Lamadrid et al. 2017]. Overall, the $\Delta\text{CO}_2\text{corr}$ measured using the single peak model versus the double peak model predict $\Delta\text{CO}_2\text{corr}$ somewhere in between liquid and vapor $\Delta\text{CO}_2\text{corr}$ on our instrument occasionally skewed high or low depending on the predominant phase peak in the intensity of the spectrum.

this bubble has been heated above T_{crit} when analyzed with a 20 mW laser power at 24 °C. However, we recognize that there is not enough data to give a conclusive answer on this specific matter.

Lastly, at 24 °C, the single peaks evident in the 20 mW spectrum are significantly closer to the position of the liquid CO_2 peak measured at 0.5 mW (e.g. $v_{2\text{pk}, \text{liquid}, 0.5\text{mW}}^-$ – $v_{1\text{pk}, 20\text{mW}}^- = 0.35\text{ cm}^{-1}$, 16 % away from $v_{2\text{pk}, \text{liquid}}^-$) than to that of the vapor peak at 0.5 mW ($v_{2\text{pk}, \text{vapor}, 0.5\text{mW}}^-$ – $v_{1\text{pk}, 20\text{mW}}^- = 1.8\text{ cm}^{-1}$, 84 % away from $v_{2\text{pk}, \text{vapor}, 0.5\text{mW}}^-$).

This is consistent with a CO_2 fluid of high density (~0.63 g mL⁻¹) close to being liquid only at 24 °C. If we consider that the total volume of the bubble ($V_{\text{tot}} = 1$) and the total mass of CO_2 in the bubble are constant, we can calculate relative phase proportions ($V_{\text{tot}} = V_{\text{liquid}} + V_{\text{vapor}} = 1$) for a bubble with a bulk density in the miscibility gap as follows:

$$V_{\text{liquid}} (\%) = 100 \times \frac{\rho_{\text{bulk}} - \rho_{\text{vapor}}}{\rho_{\text{liquid}} - \rho_{\text{vapor}}} \quad (3a)$$

$$V_{\text{vapor}} (\%) = 100 - V_{\text{liquid}} \quad (3b)$$

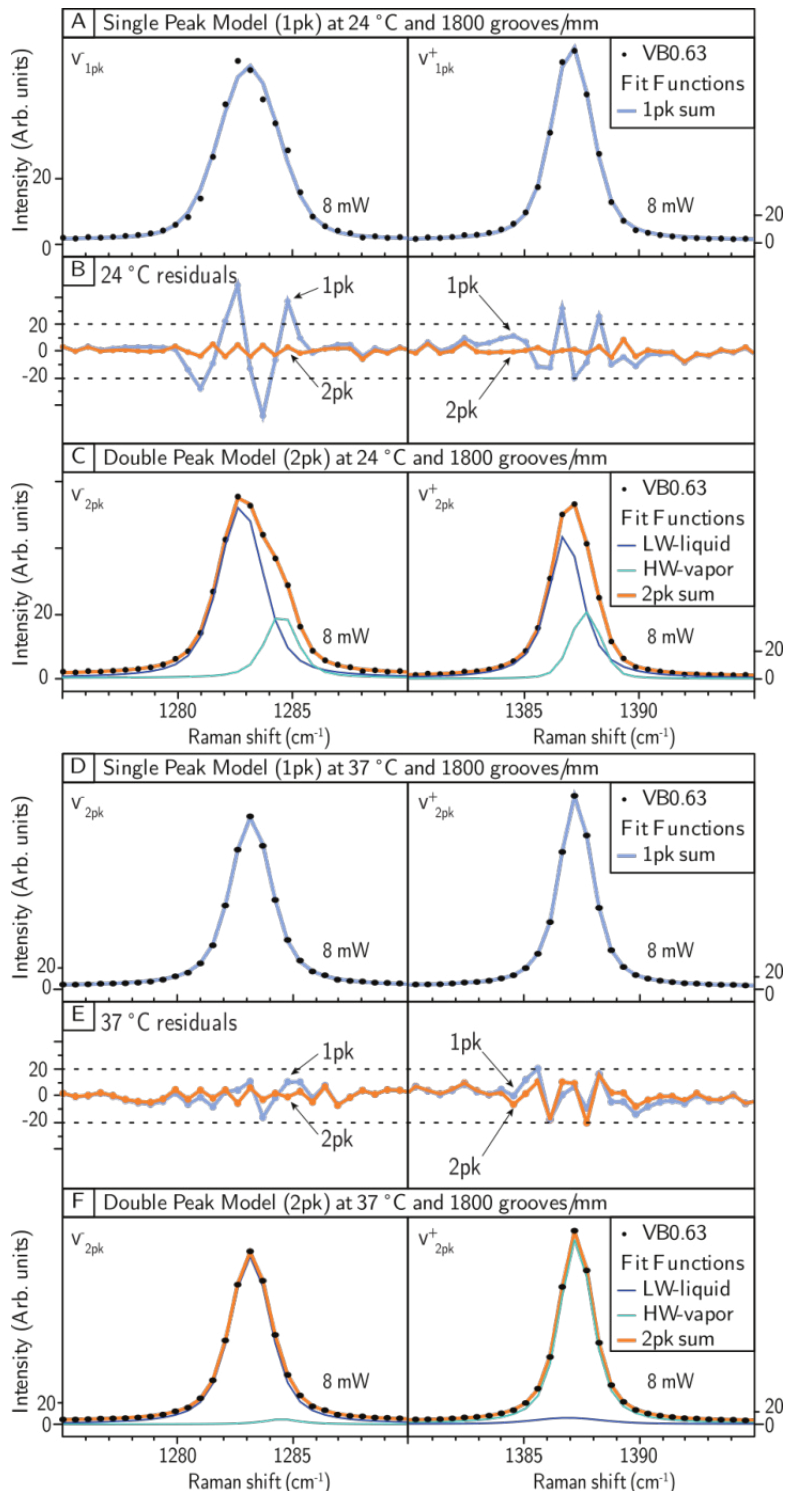


Figure 5: Peak-fitting methods and output from Fityk [Wojdry 2010], each function is only represented as points corresponding to each point on the spectrum. [A] Single Peak model fit to the 24 °C 8 mW spectrum of VB0.63 in [Supplementary Material Figure S3](#). [B] Residuals of single and double peak models on the 24 °C spectrum. [C] Double Peak model fit to the same spectrum at 24 °C. Note that acknowledging the presence of L and V phases improves the fit in terms of shape and position particularly on the v^- band (for which their contribution is naturally better resolved) and the resulting fit peaks have relative positions and intensities that are coherent when comparing v^- and v^+ . [D] Single Peak model fit to a 37 °C 8 mW spectrum of VB0.63, where all CO₂ will be found as a single supercritical phase. [E] Residuals of single and double peak models on the 37 °C spectrum. [F] Double Peak model fit to the same spectrum as [D]. The fit is not improved by adding an additional peak on either Raman bands and the relative intensity and position of the fitted peaks is incoherent: the lower wavenumber fit peak is more intense than the higher wavenumber fit peak for v^- but the opposite for v^+ .

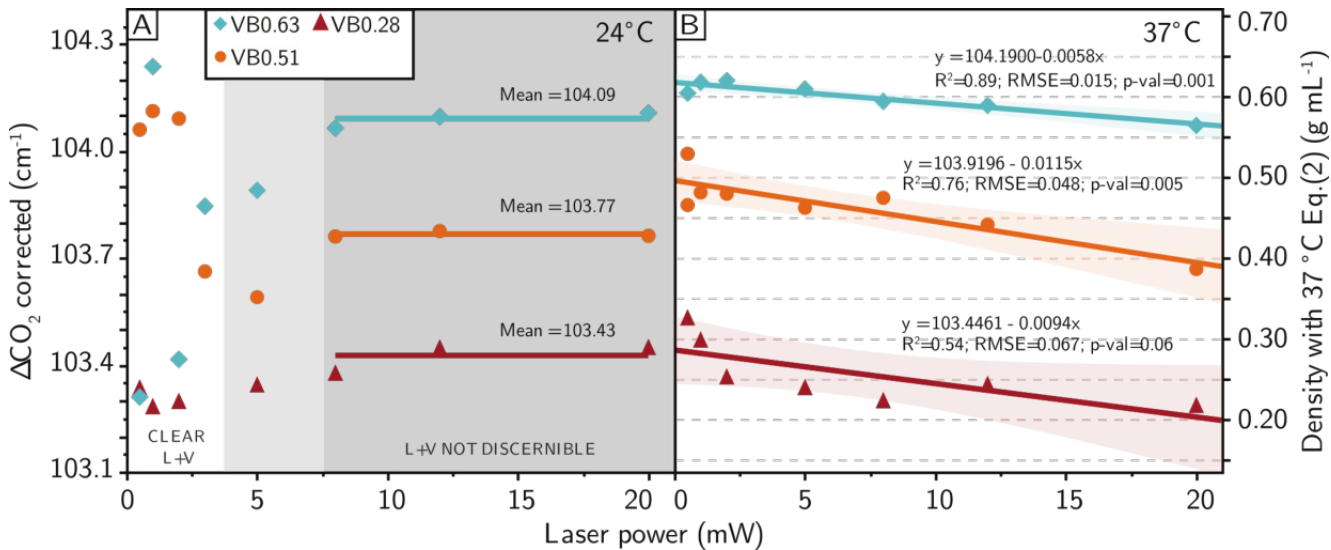


Figure 6: Effect of laser power at sample on the splitting of the Fermi diad at 24 and 37°C . All data plotted here was acquired at 1800 grooves/mm and 45 s integration time with 5 accumulations and calculated using the single peak model shown in Figure 5. [A] Laser power versus corrected CO_2 Fermi separations at 24°C and 37°C for spectra acquired at 45 s integration time and 5 accumulations with 1800 grooves/mm grating. Error bars on this plot are smaller than the symbols at laser powers >2 mW at both temperatures and the same size as the symbols for laser powers <2 mW (Supplementary Material Figure S1). At 24°C we calculated the mean of the apparent “plateau” reached after 8 mW laser power to compare to the best-fit linear intercept of the 37°C distributions. The best-fit intercept is used as the corrected value of the ΔCO_2 at 37°C (value with no laser-induced heating). The Mean ΔCO_2 measured at 24°C and laser power above 8 mW is generally lower than the one measured at low laser power at 37°C .

where ρ_{liquid} is the density of the liquid phase and ρ_{vapor} is that of the vapor phase at a specific temperature. Here, we take $\rho_{\text{liquid}} = 0.73 \text{ g mL}^{-1}$ and $\rho_{\text{vapor}} = 0.23 \text{ g mL}^{-1}$, as calculated at 24°C by the EOS of Span and Wagner [1996]. Based on its bulk density (0.63 g mL^{-1}), VB0.63 would contain approximately 81% liquid and 19% vapor by volume and is therefore predominantly composed of liquid CO_2 . It is interesting that the calculated volume proportions of each phase in the bubble at 24°C (81% liquid and 19% vapor) coincide well with the proximity of the $v_{1\text{pk}, 20\text{mW}}^-$ to the $v_{2\text{pk}, \text{liquid}, 0.5\text{mW}}^-$ (84%) in the Raman spectrum. In other words, the distance between $v_{1\text{pk}, 20\text{mW}}^-$ and the liquid and vapor peaks measured at 0.5 mW and 24°C appears proportional to the relative calculated phase proportions by volume in the bubble.

3.3 VB0.51 ($\rho_{\text{CO}_2} = 0.51 \text{ g mL}^{-1}$)

At 24°C , both liquid and vapor were identified in the spectrum collected from vapor bubble VB0.51. The 37°C analyses yielded a best-fit CO_2 density of 0.51 g mL^{-1} , which places it within the miscibility gap at T_{amb} (Figure 3D–F) but it would turn to a supercritical phase above 31°C (Figure 3E). For this bubble, separate liquid and vapor peaks are resolved in spectra collected with the 1800 grooves/mm grating (Figure 3D) and laser powers of 0.5–3 mW. Above 5 mW laser power it is challenging to resolve two phases in spectra acquired with an 1800 grooves/mm grating, but those using the 2400 grooves/mm grating (Figure 3J) are asymmetric up to 12 mW. An overall broadness and asymmetry of the 5 and 8 mW peaks (compared to the 20 mW) at 1800 grooves/mm

grating may also suggest an unresolved contribution of two-phase peaks to the band.

As with VB0.63, single-peak models applied to spectra up to 12 mW laser power do not match the spectra as well as the double-peak models that assume two phases are present. The double-peak fits yield ΔCO_2 close to the pure liquid and vapor phases of CO_2 at 24°C (Figure 4C, D). With increasing laser power, the liquid and vapor peaks move closer together until they appear to converge into a single peak between 12 and 20 mW. At 20 mW, the peaks fully merged into a single peak positioned between the independent peaks observed at 0.5 mW. Unlike VB0.63, the position of this single merged peak is approximately equidistant to that of the liquid and vapor CO_2 peaks measured at 0.5 mW ($v_{2\text{pk}, \text{vapor or liquid}, 0.5\text{mW}}^- - v_{1\text{pk}, 20\text{mW}}^- = 1.11 \text{ cm}^{-1}$, 50% away from both $v_{2\text{pk}, \text{vapor}, 0.5\text{mW}}^-$ and $v_{2\text{pk}, \text{liquid}, 0.5\text{mW}}^-$). This is consistent with a CO_2 fluid of medium density ($\sim 0.50 \text{ g mL}^{-1}$) with similar volumes of liquid and vapor coexisting at T_{amb} . For this, Equation 3 predicts ~56% liquid CO_2 and 44% vapor CO_2 by volume, which is nearly the same result as the percent proximity of $v_{1\text{pk}, 20\text{mW}}^-$ to $v_{2\text{pk}, \text{vapor}, 0.5\text{mW}}^-$ and $v_{2\text{pk}, \text{liquid}, 0.5\text{mW}}^-$.

3.4 VB0.28 ($\rho_{\text{CO}_2} = 0.28 \text{ g mL}^{-1}$)

VB0.28 (Figure 3G–I) yielded a best-fit CO_2 density of 0.28 g mL^{-1} at 37°C , and it is contained in the same olivine crystal as VB0.51 but within a different melt inclusion. As with the other samples, a bubble of this density should contain liquid and vapor T_{amb} (Figure 3D, E) and should fully

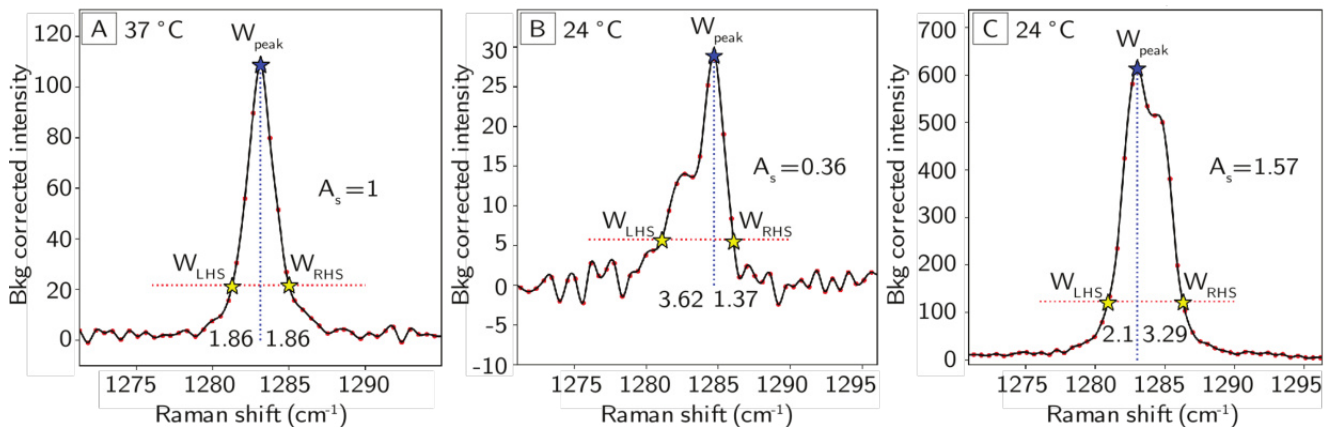


Figure 7: Asymmetry of three Raman ν^- bands from DiadFit, from the spectra of VB0.63. Background corrected intensity is plotted against Raman shift (cm^{-1}). The asymmetry factor A_s using Equation 4 in Section 3.5 [A] Symmetric ν^- band of VB0.63 acquired at 37 °C (single-phase CO₂) and 0.5 mW. [B] Fronting ν^- band of VB0.63 acquired at 24 °C and 0.5 mW (two-phase CO₂). [C] Tailing ν^- band of VB0.63 acquired at 24 °C and 5 mW (two-phase CO₂).

turn to a vapor phase above ~28 °C (Figure 3H) and to a supercritical phase above ~33 °C (Figure 3H). For this bubble, liquid and vapor peaks are challenging to resolve in spectra collected with the 1800 grooves/mm grating (Figure 3D), but they may be resolvable at the lowest laser powers, particularly at 0.5 mW. A spectrum acquired with the 2400 grooves/mm grating and 0.5 mW laser power confirms the contribution of a liquid phase. Additionally, the ν^+ CO₂ band in 0.5–5 mW analyses is asymmetric. This shape is not unlike that of the 2 mW spectrum of VB0.63 in which the vapor phase was predominantly analyzed (Figure 3A). Above 5 mW laser power, the band becomes more symmetric.

Fitting double-peak models to these spectra improves fit for 0.5, 1 and 2 mW analyses but makes no difference at higher power (Figure 4B), which could indicate that the CO₂ was entirely converted to vapor and perhaps a supercritical phase above these laser powers. At 20 mW, the single merged peak is significantly closer to the position of vapor CO₂ measured at 0.5 mW ($\nu_{2\text{pk}}^-$, vapor, 0.5 mW – $\nu_{1\text{pk}}^-$, 20 mW = 0.25 cm^{-1} , 10% away from $\nu_{2\text{pk}}^-$, vapor, 0.5 mW) than the position of the liquid peak at 0.5 mW ($\nu_{2\text{pk}}^-$, liquid, 0.5 mW – $\nu_{1\text{pk}}^-$, 20 mW = 2.2 cm^{-1} , 90% away from $\nu_{2\text{pk}}^-$, liquid). This is consistent with a CO₂ fluid of relatively low density (~0.28 g mL⁻¹) where little liquid is found at T_{amb} . In this case Equation 3 predicts ~10% liquid CO₂ and 90% vapor CO₂ by volume for a bubble with a bulk density of 0.28 g mL⁻¹, and this is the same result as the percent proximity of $\nu_{1\text{pk}}^-$, 20 mW to $\nu_{2\text{pk}}^-$, vapor, 0.5 mW and $\nu_{2\text{pk}}^-$, liquid, 0.5 mW.

3.5 Relationships between peak asymmetry and laser power

As mentioned in Sections 4.1–4.3, it is often difficult or impossible to visually identify the contribution of more than one phase in spectra collected at laser powers greater than 5 mW. This is particularly true when the spectral resolution is lower than 0.3 cm^{-1} , as in our case when using a common setup of 1800 grooves/mm grating and 532 nm laser (~0.54 cm^{-1} spectral resolution on the Cornell and Berkeley instruments). How-

ever, in these analyses, a broadness or asymmetry of the peak is often noticeable. To explore the relationship between peak broadness and asymmetry with laser power and analysis time, we have developed a Python3 peak fitting routine included in the python tool DiadFit v0.0.57 [see Data Availability; Wieser and DeVitre 2023] to quantify peak asymmetry. This routine uses the band asymmetry factor (A_s), a proxy widely used in chromatography to assess the quality of separation of components [see Supporting Information for an example Jupyter Notebook; Berruex and Freitag 2003]. First, we perform a linear baseline subtraction on either side of each diad and then fit a cubic spline through the data. We identify the wavenumber (W_{peak}) and intensity of the center of the highest peak, and then identify the wavenumber of the points with an intensity 20% of the W_{peak} on the left shoulder (W_{LHS}) and right shoulder (W_{RHS}). The band asymmetry factor A_s is defined as the distance between these shoulder and peak positions:

$$A_s = \frac{W_{\text{RHS}} - W_{\text{peak}}}{W_{\text{peak}} - W_{\text{LHS}}}. \quad (4)$$

A ratio of 1 would indicate perfect symmetry of the band, more likely to represent a pure single-phase (Figure 7A, 0.5 mW spectra at 37 °C).

We expect that when more than one phase contributes to the spectrum, significant asymmetry should be detected (Figure 7B, 0.5 mW spectra at 24 °C), where a ratio < 1 would represent a fronting band (e.g. vapor peak intensity $>$ liquid peak intensity, Figure 7B) and a ratio > 1 would indicate a tailing band (liquid peak intensity $>$ vapor peak intensity, Figure 7C). Note that the symmetry of bands may differ between instruments due to hardware differences such as the pinhole size, and “acceptable” levels of asymmetry should be assessed on each instrument and against known single-phase spectra (i.e. a pure liquid, pure vapor, or supercritical CO₂ spectrum). As expected, for each bubble at 37 °C (all CO₂ found as a single supercritical phase) A_s is constant and near 1 regardless of laser power ($A_s = 0.96 \pm 0.01$ (SD), 1.28 ± 0.02 , 1.07 ± 0.04 for VB0.63, VB0.28, and VB0.51 respectively).

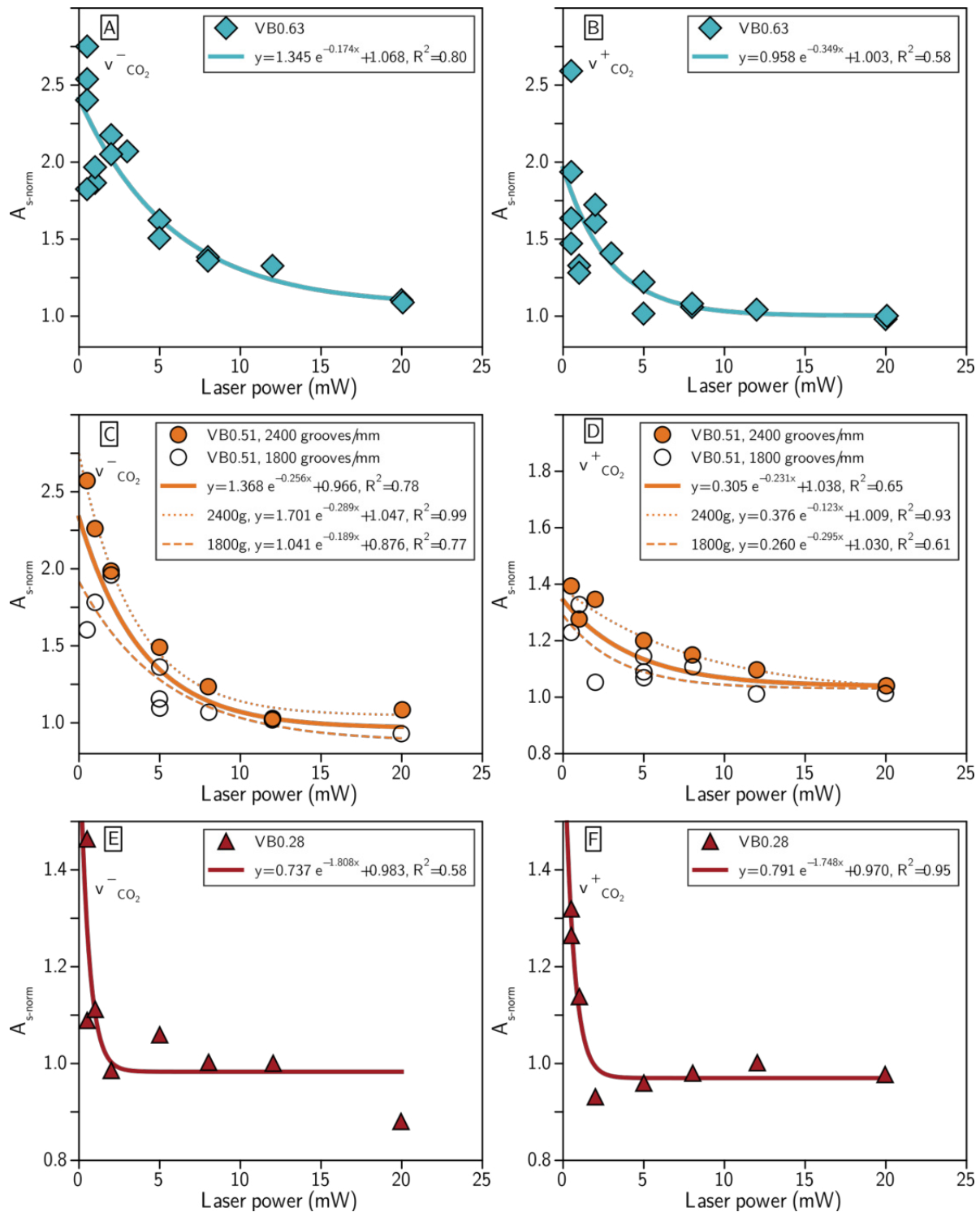


Figure 8: Laser power versus maximum band asymmetry factor A_{s-norm} for each vapor bubble for the 24 °C data ($A_{s-24°C}$) normalized to the 37 °C data ($A_{s-37°C}$) using Equation 5 in Section 3.5. An exponential function is fit through the data. [A-B] A_{s-norm} as a function of laser power for v^- and v^+ bands of VB0.63. [C-D] A_{s-norm} as a function of laser power for v^- and v^+ bands of VB0.51. For this bubble, three equations were fit: one for 1800 grooves/mm data only (dashed line), one for 2400 grooves/mm data only (dotted line) and one for both datasets together (solid line). The fit on the 2400 grooves/mm data is significantly better than the 1800 grooves/mm owing to the higher spectral resolution of the data ($R^2 = 0.99$ versus 0.76). [E-F] A_{s-norm} as a function of laser power for v^- and v^+ bands of VB0.28. As laser power increases, the symmetry for the two Raman bands also increases and converges towards the mean A_{s-norm} at 37 °C for all three bubbles. Symmetry appears to be achieved at the relative lowest laser power for VB0.28 and at the relative highest for VB0.63. Error bars are generally smaller than the symbols for laser powers between 5 and 20 and similar to or slightly larger than the symbols for laser powers < 5 mW, but do not change the trends (see Supplementary Material Figure S2).

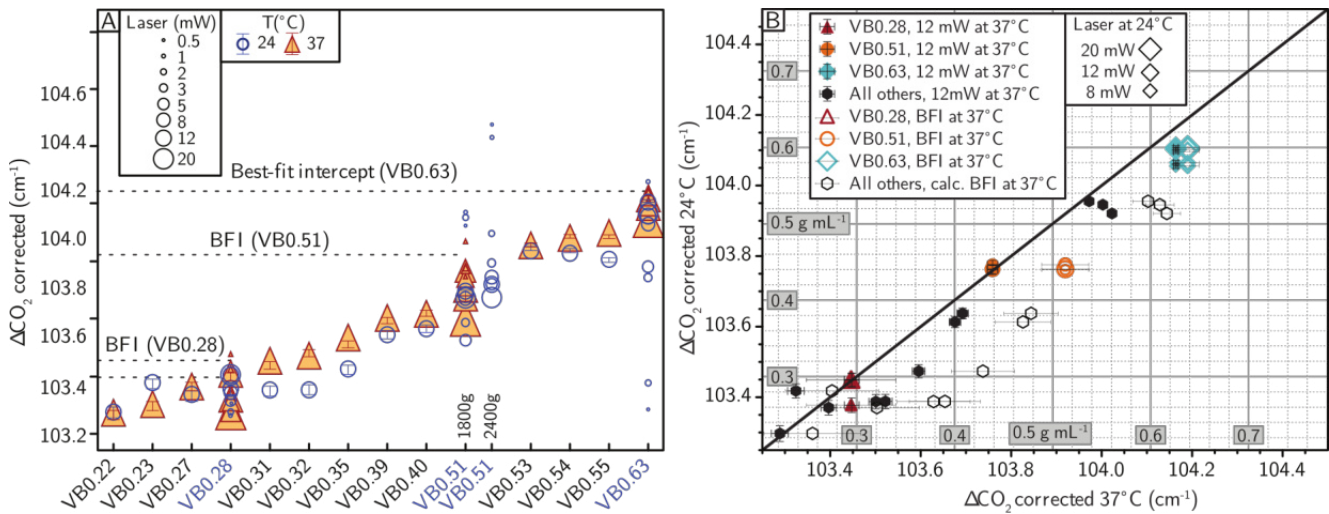


Figure 9: $\Delta\text{CO}_{2\text{corr}}$ of all the bubbles measured in this study acquired at 45 s integration time and 5 accumulations at both 24 and 37 °C, 1800 and 2400 grooves/mm grating. [A] Symbols are sized by laser power. Triangles are for 37 °C data and circles for T_{amb} data. The 2400 grooves/mm data are shifted using a constant of 0.15 cm^{-1} corresponding to the difference between the 20 mW $\Delta\text{CO}_{2\text{corr}}$ at 1800 and 2400 grooves/mm. Error bars for VB0.28, VB0.51 and VB0.63 are calculated as standard deviation of the mean for 12 mW acquisitions at both temperatures by two different Raman operators; error bars for all other samples are linearly extrapolated from the former. Overall, $\Delta\text{CO}_{2\text{corr}}$ measured at 12 mW and 24 °C are underestimated when compared to the $\Delta\text{CO}_{2\text{corr}}$ measured at 37 °C particularly for vapor bubbles with bulk densities near 0.5 g mL^{-1} and $\Delta\text{CO}_{2\text{corr}}$ comprised between 104.0 and 103.45 cm^{-1} . For such bubbles, estimates of the $\Delta\text{CO}_{2\text{corr}}$ made at 24 °C show significant scatter and unpredictability depending on laser power. This effect is less important for bubbles close to being either pure liquid or vapor at T_{amb} . [B] $\Delta\text{CO}_{2\text{corr}}$ measured at 24 °C (sized by 8–20 mW) versus $\Delta\text{CO}_{2\text{corr}}$ measured at 37 °C (12 mW and best-fit intercept or BFI) in each vapor bubble. Error bars on measured samples are the same as in [A]. The grid corresponds to densities as calculated by Equation 2, applied to both 24 °C data (horizontal lines) and 37 °C data (vertical lines). The 1:1 line indicates when $\Delta\text{CO}_{2\text{corr}}$ measured at 24 °C is identical to the $\Delta\text{CO}_{2\text{corr}}$ measured at 37 °C and 12 mW laser power on sample. Empty symbols indicate best-fit intercepts for 3 known bubbles (Figure 6). For all other vapor bubbles, best-fit intercepts are calculated using a 2nd degree polynomial regression of slopes versus densities based on the regression lines in Figure 6. These are only meant to illustrate a possible underestimation brought about by laser heating on samples other than the three on which detailed experiments were conducted. Error bars on Best-Fit Intercepts for VB0.28, VB0.51 and VB0.63 are calculated as the uncertainty on the intercept from each regression (Figure 6) and the uncertainty for all other BFI is a linear extrapolation of these three.

As the allocation of the numerator and denominator in Equation 4 is arbitrary, for all subsequent calculations, we define A_s as the ratio of the longest direction between the peak and the shoulder to the shortest, so that it always represents a maximum band asymmetry factor regardless of direction. Further, given that A_s at 37 °C was found to be constant for each bubble at different laser powers, we normalize A_s at 24 °C ($A_s^{24\text{ °C}}$) to the mean A_s at 37 °C ($\overline{A_s^{37\text{ °C}}}$) for each bubble in Figure 8 and report the maximum normalized asymmetry band factor as:

$$A_{s\text{-norm}} = \frac{A_s^{24\text{ °C}}}{\overline{A_s^{37\text{ °C}}}}. \quad (5)$$

To avoid issues related to excessive noise, we excluded any spectra with integration times below 30 s and those acquired with fewer than 3 accumulations from the analysis plotted in Figure 8 (Supplementary Material Figure S2 shows typical precision of measurements). A few examples of high noise spectra can be seen in Supplementary Material Figure S5. Yuan and Mayanovic [2017] show that for narrow intense spectra (Intensity/FWHM $> \sim 200 \text{ counts cm}^{-1}$) fitting error

is typically $< 0.03 \text{ cm}^{-1}$ when the spectral resolution is $0.8\text{--}1 \text{ cm}^{-1}$. Intensity/FWHM for spectra acquired with 45 s and 5 accumulations is systematically well over 200 counts cm^{-1} and although 30 s and 3–5 accumulations can be smaller (50–100 counts cm^{-1}) we consider it is reasonable to include such spectra given that the fitting error is likely smaller for our data because the spectral resolution is $\sim 0.54 \text{ cm}^{-1}$.

With increasing laser power, the $A_{s\text{-norm}}$ of both the v^- (Figure 8A, C, E) and v^+ (Figure 8B, D, F) bands of CO₂ decreases exponentially (3-parameter fit). At lower laser powers, $A_s^{24\text{ °C}}$ is significantly larger than $A_s^{37\text{ °C}}$ but converges towards $A_s^{37\text{ °C}}$ as laser power increases (Figure 8). This exponential decrease in the asymmetry of the Raman bands is particularly strong for VB0.63 and VB0.51 but is also observed at low laser power for VB0.28. For VB0.51, we fit 3 separate exponential functions: (1) through spectra acquired with the 2400 grooves/mm grating only, (2) through spectra acquired with the 1800 grooves/mm grating only, and (3) one through the compilation of both datasets. While all the fits are significant, the fit on the 2400 grooves/mm data is notably better ($R^2 = 0.99$) than the fit on the 1800 grooves/mm data ($R^2 = 0.76$), because of the higher spectral resolution of this grating.

3.6 Integration time and accumulations

It could be hypothesized that at a given laser power, longer analysis times (longer exposure to the laser) could result in increased heating. To test the effects of integration time and accumulations on our results, VB0.51 was analyzed at different integration times and accumulations at 0.5 mW (45 s \times 5 accumulations, 90 s \times 5 and 200 s \times 3), 5 mW (5 s \times 1, 5 s \times 5, 10 s \times 1, 10 s \times 3, 20 s \times 1, 45 s \times 1, 10 s \times 5, 30 s \times 3, 90 s \times 1, 45 s \times 5), and 10 mW (5 s \times 1, 10 s \times 1, 5 s \times 5, 20 s \times 1, 10 s \times 3 and 10 s \times 5). However, we found no discernable differences in our results after a given amount of time (see [Supplementary Material Figure S5](#)).

4 DISCUSSION

4.1 Evidence for laser-induced heating of melt inclusion vapor bubbles

Our results show that laser power influences the shape and position of the CO_2 ν^+ and ν^- Fermi diad peaks, and in turn the estimated $\Delta\text{CO}_{2\text{corr}}$. The most likely cause of these changes is laser induced heating of the vapor bubble.

The critical observation is that at the lowest laser power (0.5 mW) both the liquid and vapor peaks of CO_2 can be clearly resolved in the Raman spectra of all three bubbles ([Figure 3A, D, G, J–L](#)), and as laser power increases the liquid and vapor peaks converge until they are eventually indistinguishable at 20 mW laser power. This convergence is consistent with the expected effect of increasing temperature on liquid and vapor CO_2 phase stability ([Figure 1B, C](#)). For example, the CO_2 phase diagram shows that at 20 °C and relevant pressure, CO_2 with a density below 0.19 g mL $^{-1}$ will exist as vapor while that with a density >0.77 g mL $^{-1}$ will exist as liquid. If the CO_2 bulk density is between these values (i.e. in the miscibility gap), it will co-exist as a 0.77 g mL $^{-1}$ liquid and a 0.19 g mL $^{-1}$ vapor. At 28 °C and CO_2 density in the miscibility gap, the co-existing phases would be a 0.29 g mL $^{-1}$ vapor and a 0.66 g mL $^{-1}$ liquid. This shows that the $\Delta\text{CO}_{2\text{corr}}$ of the liquid phase, and thus the calculated density, should decrease with increasing temperature (i.e. peak positions move to higher wavenumbers), while the $\Delta\text{CO}_{2\text{corr}}$ and density of the vapor phase should conversely increase with increasing temperature (i.e. peak positions move to lower wavenumbers). In other words, the result of increasing temperature is that the vapor and liquid CO_2 peaks should converge, and this is what we observe with increasing laser power in our 24 °C experiments ([Figure 3A, D, G, J, Figure 4](#)).

Our laser heating hypothesis is also supported by the results from experiments at 24 °C and 37 °C. First, we find no significant relationship between A_s and laser power in 37 °C experiments ($A_s = 0.96 \pm 0.01$ (SD), 1.28 ± 0.02 , 1.07 ± 0.04 for VB0.63, VB0.28 and VB0.51 respectively). This observation is consistent with the presence of a single homogeneous phase at 37 °C (i.e. above T_{crit}). Second, with increasing laser power, the A_s of 24 °C spectra decrease towards the mean A_s of the 37 °C spectra ([Figure 8](#)). Therefore, with increasing laser power, the A_s at 24 °C converges towards the single-phase 37 °C A_s for each sample.

Finally, it is worthwhile to note that the Fermi diad separation and the position of the peaks are independent of laser power when laser power does not induce any significant changes in the fluid temperature. For example, in a relatively large volume calibration apparatus such as the one used by [DeVitre et al. \[2021\]](#), the maximum temperature change observed when the laser is on is at most 0.02–0.03 °C even with 60 mW laser power at sample.

Overall, these results suggest that the increase in laser power is increasing the temperature of the vapor bubble such that the density of the liquid and vapor phases varies in accordance with increasing temperature on the phase diagram, and the liquid and vapor Raman peaks converge until the bubbles contain a single phase only. This helps explain why even calibrated T_{amb} measurements of natural samples sometimes give densities in the miscibility gap, whereas those from gas-cell calibration apparatus do not: natural inclusions are characterized by exceedingly small ($\sim 1 \times 10^3 \mu\text{m}^3$) and closed volumes, while the calibration apparatus has a much larger volume ($\sim 1 \times 10^{12} \mu\text{m}^3$). Thus, the potential for laser heating is much greater in natural inclusions than in a calibration apparatus. However, even in natural samples, the amount of heating induced by the laser is likely much lower for melt inclusions than the models of [Hagiwara et al. \[2021\]](#) suggested for pure fluid inclusions, as two phases were still identified at 12 mW for at least two of our analyzed bubbles. We note that an argument for an effect of laser heating on a specific set of samples can only be made after an instrument specific calibration has been performed to rule out overestimations caused by using densimeters calibrated on other instruments or when a set of experiments on a specific bubble at different laser powers have been conducted and relationships have been established.

4.2 Uncertainties in the measurement of the Fermi diad separation and CO_2 densities due to laser-induced heating

Our results have implications for how Raman analyses should be conducted, how Raman data should be processed, and how uncertainties are estimated on density results. When the laser heating effect is strong, the liquid and vapor phase contributions are nearly indistinguishable in the spectrum, particularly at lower spectral resolution (e.g. 12–20 mW analyses in [Figure 3A, D, G, J](#)). In such cases, a single peak fit to each band can produce a $\Delta\text{CO}_{2\text{corr}}$ and calculated density within the miscibility gap ([Figures 4, 6A, and 9](#)), though this density could still be significantly underestimated (0.03–0.05 g mL $^{-1}$) relative to that obtained at 37 °C, particularly for vapor bubbles with bulk densities of 0.3–0.7 g mL $^{-1}$. It is also possible, as suggested by [Hagiwara et al. \[2021\]](#) for fluid inclusions, that high power lasers can cause heating on the order of tens of degrees in the bubble, which would drag the temperature significantly above T_{crit} , and thus, CO_2 would become a single supercritical phase. However, as they also suggest, heating could cause an underestimation of the density that should be corrected when possible either via experiments on relevant bubbles and inclusions or by estimating the laser heating coefficient for each sample using a densimeter calibrated at multiple temperatures.

Densimeters are calibrated at specific pressure-temperature conditions and the calibration relies on the relationship between density and the separation of the Fermi diad given the relative volume of the optical cell, and under the assumption that temperature and laser-induced heating do not significantly affect the Fermi diad separation. However, it has been shown that temperature influences the peak positions and the separation of the Fermi diad [Wang et al. 2011; Yuan and Mayanovic 2017; Wang et al. 2019; Sublett et al. 2020; DeVitre et al. 2021] mainly due to changes in the attractive and repulsive forces between molecules and thermal expansion. Therefore, this effect should be considered when performing calibrations and Raman analysis of natural fluid and melt inclusions. Indeed, if the Fermi diad splitting is less than expected for a specific density due to laser heating, this would in turn result in an underestimation of the calculated density of CO₂.

The effect of a relatively small (i.e. T_{amb} to 37 °C) temperature change on the separation of the Fermi diad is negligible for densities of CO₂ below 0.1 g mL⁻¹ [see Figure 8 in DeVitre et al. 2021] and limited for densities above 0.8 g mL⁻¹, but, in the miscibility gap (0.2–0.7 g mL⁻¹ at T_{amb}), the effect can be significant and can only be assessed above T_{crit} . As temperature increases, the measured splitting decreases, so by using a calibration equation acquired at a lower temperature than the measurement temperature (as in the case of laser heating), one would naturally end up underestimating the density of the measured CO₂. It has been hypothesized that these differences in peak position and Fermi splitting are due to changes in the intermolecular attractive and repulsive forces [Sublett et al. 2020] where an isobaric increase in the temperature up until a certain point (well above 400 °C) coincides with a predominance of repulsive forces [this is clearly shown in figures 1 and 3 of Sublett et al. 2020]. The result of this effect is an increase in the peak positions of the diad and a slight decrease in the Fermi separation. Note that this behavior is opposite of that brought about by an isothermal increase in pressure and density for which the peak positions move to lower wavenumbers—and the Fermi separation increases—up until an inflection point [well above 100 MPa; Sublett et al. 2020]. Another suggested explanation proposes that the change in Fermi splitting is due to small volume changes induced by thermal expansion or contraction of the host or vessel [Hagiwara et al. 2018; 2021]. However, it is mechanically unlikely that a difference of only ~13 °C between 24 and 37 °C might cause any significant change in the volume of the bubble and/or calibration vessel (<0.05 % with a typical 316 Stainless Steel thermal expansion coefficient of $16 \times 10^{-6} \text{ K}^{-1}$). Further, in the case of a calibration apparatus, any significant change in volume would be recorded as a pressure change during the experiment.

As mentioned, it would be challenging to assess if, when, and by how much T_{crit} has effectively been surpassed from ΔCO_2 measurements done at T_{amb} . We note that when peaks are found to be significantly asymmetric relative to peaks that are expected to correspond to pure phases, this could be indicative that T_{crit} has not been reached. While hot band thermometers could give insight into the temperature of va-

por bubbles during analysis, these typically have high uncertainty (± 4 °C—unacceptable for bulk densities in the miscibility gap near the critical temperature) and are calibrated only in fluid inclusions above approximately 0.68 g mL⁻¹ [Brown and Steeper 1991; Rosso and Bodnar 1995; Arakawa et al. 2008; Hagiwara et al. 2018; 2021]. Below this, and particularly in lower density natural samples, the signal-to-noise ratio of the hot bands is often not large enough to provide a reliable fit and a meaningful estimate of temperature. For instance, a calculation of the intra-analysis temperature of one of our vapor bubbles (0.63 g mL⁻¹) using the Hagiwara et al. [2018, 2021] hot-band thermometer—which has a reported uncertainty of at least ± 3.8 °C—predicts a temperature of ~55–70 °C for laser powers of 8–20 mW; however, even within the reported uncertainty, this is inconsistent with the presence of liquid and vapor phase peaks in the spectra of our vapor bubble acquired at 8–12 mW (Figure 5A) which indicates that temperature of the bubble has not exceeded T_{crit} .

Our experiments at 37 °C show a decrease in the measured $\Delta\text{CO}_2_{\text{corr}}$ with increasing laser power (Figure 6A, 37 °C), consistent with the experiments of Hagiwara et al. [2021] in fluid inclusions hosted in olivine. Indeed, the $\Delta\text{CO}_2_{\text{corr}}$ for VB0.63 measured at 12 mW is ~0.06 cm⁻¹ lower than the best-fit intercept (Figure 6A, 37 °C) and the measured $\Delta\text{CO}_2_{\text{corr}}$ at 1 and 2 mW, which amounts to ~0.03 g mL⁻¹ or 5 % underestimation of the density. At 20 mW, the decrease corresponds to ~0.12 cm⁻¹ and an underestimation of the density of the bubble of ~0.06 g mL⁻¹ or ~10 %. For VB0.51 the decrease is ~0.12 cm⁻¹ at 12 mW (~0.06 g mL⁻¹ or ~12 %) and ~0.25 cm⁻¹ at 20 mW (~0.11 g mL⁻¹ or ~23 %). For VB0.28, hosted in the same crystal as VB0.51, the decrease is ~0.04 cm⁻¹ at 12 mW (~14 %) and ~0.065 cm⁻¹ at 20 mW (~23 %). Figure 12b in DeVitre et al. [2021] shows how the uncertainty in the density of vapor bubble can affect the calculated total CO₂ content of a melt inclusion depending on the bubble volume fraction and the density of the bubble. How this, in turn, affects calculated saturation pressures will depend on the composition of the melt and solubility model that is chosen.

4.3 Implications for the uncertainties in calculated saturation pressures and MI entrapment depths

To illustrate the effect of laser-heating associated uncertainty on calculated saturation pressures and depths of entrapment, we perform calculations assuming 80 % of the CO₂ is contained in bubbles with volume fractions of 2, 4 and 6 %. For the sake of this exercise, we assume mafic alkaline compositions for the melt (Etna composition from Allison et al. [2019]) with a predominance of CO₂ over H₂O in the fluid ($X_{\text{CO}_2} > 80\%$) and we calculate all saturation pressures using the MagmaSat solubility model Ghiorso and Gualda [2015] implemented in VESIcal 1.2.0 [Iacovino et al. 2021; Wieser et al. 2022]. The choice of solubility model may have a significant impact on calculated saturation pressures and associated uncertainties, particularly at high pressure (>5 kbar) and high CO₂ concentrations in silica undersaturated (alkaline) melts where experiments are sparse to non-existent (Buso et al. [Thibault and Holloway 1994; Dasgupta et al. 2007; Iacovino et al. 2021; Buso et al. 2022]). A discussion of appropriate solubility models is be-

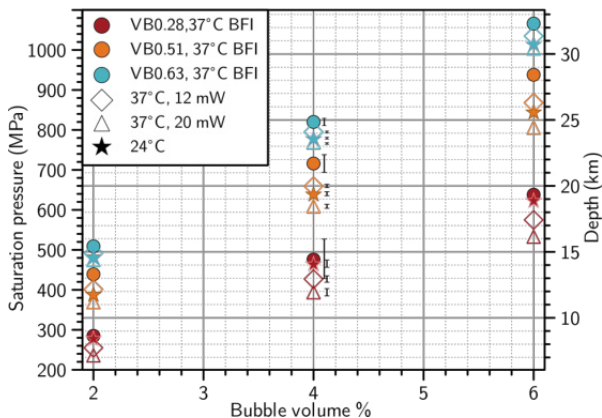


Figure 10: Calculated saturation pressures for the MI containing VB0.28, VB0.51 and VB0.63 as a function of bubble volume %. Filled circles are calculated using the accepted values of the densities when measured at 37 °C (Best-fit intercepts). Empty diamonds and empty triangles represent the underestimation equivalent to using, respectively, 12 mW and 20 mW laser powers at sample at 37 °C. Stars represent the underestimation brought about by using the plateau value of $\Delta\text{CO}_{2\text{corr}}$ measured at 24 °C. Error bars shown here are propagated uncertainties in the density alone (not considering solubility model or bubble volume % uncertainty) based on Figure 9, BFI intercept errors and measurement errors are offset from each other for clarity.

yond the scope of this study, but we choose MagmaSat here for its wider compositional and pressure range in the calibration dataset.

First, we compare the effects of using different laser powers (12 and 20 mW) at 37 °C (i.e. above the critical temperature for CO₂). If we consider a bubble with the density of VB0.63 (0.63 g mL⁻¹), an underestimation of 0.03 g mL⁻¹ or ~5% in the bubble density (equivalent to using the 12 mW laser at 37 °C, Figure 9A–B) would amount to a 300–900 ppm CO₂ underestimation. Assuming the pressure gradient is ~30 MPa km⁻¹, this would amount to an ~3% uncertainty in the entrapment pressure (~20–30 MPa) and corresponding depth (~0.5–1 km) estimates. In turn, an underestimation of 0.06 g mL⁻¹ (~10%) in the bubble density (equivalent to using 20 mW at 37 °C, Figure 9) would amount to a 500–1800 ppm CO₂ underestimation or 35–65 MPa and 1–2 km in depth (~6%, Figure 10). For VB0.51 (0.51 g mL⁻¹) and VB0.28 (0.28 g mL⁻¹), using a laser power of 12 mW laser at 37 °C respectively causes an underestimation of ~12% and ~14% in the CO₂ density, and ~8% and 10% in the entrapment pressure and depth. Using 20 mW laser power would amount to an underestimation of ~22% and ~23% in the density and ~15% and 17% in the entrapment pressure and depth.

We can perform a similar exercise comparing our data acquired at 24 °C and 37 °C. For this, we consider $\Delta\rho_{37-24\text{°C}}$ to be the difference between the density calculated by Equation 2 using the best-fit intercept of $\Delta\text{CO}_{2\text{corr}}$ at 37 °C (taken as our accepted value for each bubble) and that calculated using the mean value of $\Delta\text{CO}_{2\text{corr}}$ when an apparent plateau has been reached using >8 mW laser power at 24 °C (Figure 6).

For VB0.63 (0.63 g mL⁻¹), $\Delta\rho_{37-24\text{°C}}$ is ~0.05 g mL⁻¹ or ~8% (Figure 9B). This amounts to an underestimation of ~500–1500 ppm CO₂ (~8%), corresponding to an ~5% underestimation in entrapment pressure (30–50 MPa) and depth (1–1.5 km; Figure 10). For VB0.51 (0.51 g mL⁻¹), $\Delta\rho_{37-24\text{°C}}$ is ~0.08 g mL⁻¹ (~16%) amounting to ~11% underestimation in the entrapment pressure and the depth. Interestingly, for VB0.28, the density underestimation is only 0.01 g mL⁻¹ (3.6%), such that no significant underestimation (~2.5% in the depth) would be made by analyzing this bubble at relatively high power on the Cornell instrument (12–20 mW) and 24 °C compared to the best-fit intercept at 37 °C. Note that for VB0.63 and VB0.51, the underestimation caused by using the plateau $\Delta\text{CO}_{2\text{corr}}$ at 24 °C is similar to that caused by using 12 mW laser power at 37 °C and always less than 3 km in depth (~11%; Figure 10).

Importantly, in the specific range of our study, the uncertainties in the depth of entrapment likely caused by a laser heating effect are no larger than ~10% when vapor bubbles are analyzed at 12 mW laser power and 37 °C (Figure 10) or at 12–20 mW laser power at 24 °C. This uncertainty is likely acceptable for most studies and within error when considering other sources of uncertainty in melt inclusion analyses, such as volume estimations [Tucker et al. 2019; Mironov et al. 2020] and the choice and calibrated range of solubility models [Wieser et al. 2022].

4.4 Suggested protocols for the study of CO₂ bubbles in melt inclusions

Because it is not always straightforward to identify the presence of liquid + vapor in melt inclusion vapor bubbles due to microscope capabilities (e.g. effects of heating by microscope light vary), the use of high laser powers during analyses, exact laser position in the bubble, low signal/noise ratios and/or insufficient spectral resolution. One possibility is to always conduct exploratory scans at T_{amb} and low laser power (0.5–1 mW) on melt inclusion vapor bubbles to identify the presence of liquid and vapor. However, even when performing these exploratory scans, the presence of a very small quantity of liquid could be missed for bulk densities close to single-phase vapor at T_{amb} (e.g. VB0.28). Considering this and the added time required to conduct additional analyses on every vapor bubble, it may be safer to perform all analyses while heating above T_{crit} and at relatively low laser power at sample (<5–8 mW) to ensure that any liquid + vapor that could be present at T_{amb} has been turned into a single supercritical phase. To this effect, a Peltier stage (see diagram in Supplementary Material), composed of the Peltier module with a center hole (~\$30–40), crocodile cables, a DC power supply (\$50–70), and a thermocouple or thermistor thermometer (<\$100) can easily be built for any Raman system for less than \$200, with all components easily obtained online. A summarized workflow is shown in Figure 11.

While it is possible to turn a liquid + vapor bubble to a single phase using a high laser power at T_{amb} , this is less ideal, as it is challenging to assess when it may have fully turned to single phase, and overheating can also yield spurious densities. It is currently impossible to assess the temperature reached

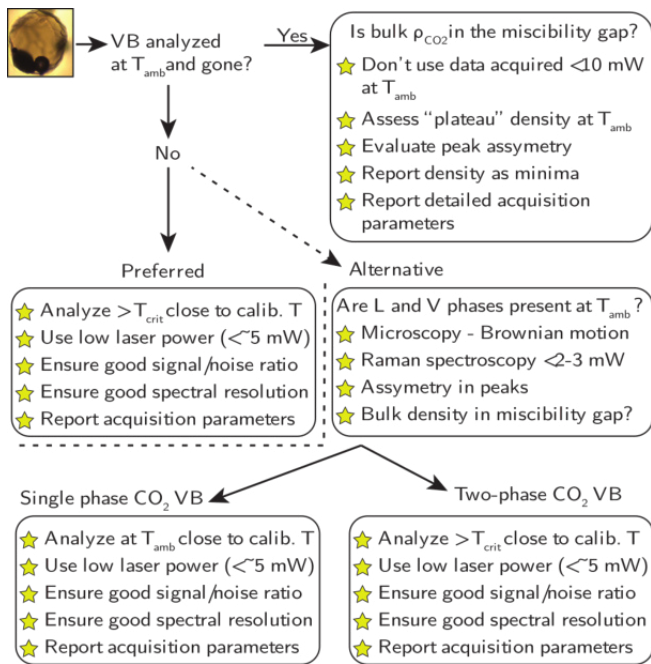


Figure 11: Summary protocol for analyzing melt inclusion vapor bubbles via Raman spectroscopy to avoid issues with laser-induced heating, particularly for vapor bubbles with CO₂ bulk densities in the miscibility gap at T_{amb} .

inside the bubble during analysis. Additionally, it is difficult to know what laser power would be required to reach the critical temperature, because the effects of the size and composition of the melt inclusion glass, the size and bulk density of the bubble, and the position of the bubble relative to the melt and host, are not constrained. These are likely important factors because heating models calibrated on pure fluid inclusions seem to significantly overpredict temperature when applied to melt inclusions. Additionally, Hagiwara et al. [2021] concluded that one of the main factors controlling the intensity of laser-induced heating could be the composition of the crystal host (i.e. their absorption coefficient) and suggest that even relatively small differences in host composition (e.g. zoning) could produce appreciable differences. A significant amount of scatter in the measured $\Delta\text{CO}_{2\text{corr}}$ can result from analyzing bubbles at T_{amb} (Figures 6 and 10) particularly for those with bulk densities in the miscibility gap that are not very close to liquid nor vapor. Furthermore, even when measuring such bubbles at 12 mW, our data shows that data collected at T_{amb} underestimates the $\Delta\text{CO}_{2\text{corr}}$ of the bubbles when compared to results from measurements above T_{crit} at the same laser power and to the best-fit intercepts from Figure 6.

Ultimately, we suggest analyzing bubbles at the lowest laser power possible (where peaks are still sufficiently strong to fit precisely), while maintaining the temperature above T_{crit} to ensure that all CO₂ in the bubble is in a single phase. Indeed, heating induced by a power of $\sim 2-3$ mW at sample is predicted to cause no more than 5% underestimation in our 3 bubbles while 5 mW keeps them within 5–10%. In turn, the best-fit linear regressions (Figure 6A) predict up to 20–40% underestimation in the density of a 0.51 g mL⁻¹ bubble, 15–

30% for a 0.63 g mL⁻¹ and 10–20% for a 0.28 g mL⁻¹ bubble when analyzed at 12–20 mW laser power. When analyzing at 24 °C and laser power at sample of 12–20 mW, we calculated that the density will be underestimated by ~8% for a 0.63 g mL⁻¹ bubble, ~16% for a 0.51 g mL⁻¹ bubble and ~3% for a 0.28 g mL⁻¹ bubble.

When identifying the approach to use, however, the analyst should consider their needs. We found that for melt inclusion bubbles with bulk densities in the miscibility gap, the maximum underestimation in the depth of entrapment that we calculated from data acquired using a high laser power (12–20 mW) at 24 °C was about 5–15%. In some cases, it may not be possible to analyze melt inclusion vapor bubbles that lie in the miscibility gap while heating above T_{crit} (e.g. all analyses have already been conducted and the vapor bubbles have been polished through during subsequent sample preparation). Given that a plateau appears to be reached at T_{amb} when MI bubbles are analyzed with laser powers above 10 mW (Figure 6), we may consider that data acquired with such laser powers, and when a plateau has been observed for a bubble analyzed on a specific instrument, could be sufficiently close to the bulk density of the bubble to provide at least a reasonable—albeit underestimated—measurement of the bulk MI bubble density. Users should confirm whether a plateau is reached on their specific instrument at increasing laser power on sample before reporting such data. In addition, raw spectra should be provided to assess peak asymmetry, acquisition conditions (laser power at sample, integration times, and accumulations) should be clearly reported, and the data should be considered minima.

Finally, for bubbles with bulk densities in the miscibility gap, we strongly discourage the use of any data acquired at laser powers below 10 mW at T_{amb} (particularly with insufficient spectral resolution) to calculate saturation pressures as a significant underestimation can occur: >0.05 g mL⁻¹ for a 0.28 g mL⁻¹ bubble (>3 km, 17%), >0.1–0.15 g mL⁻¹ for a 0.51 g mL⁻¹ bubble (>3–6 km, >15–20%) and ~0.15 g mL⁻¹ for a 0.63 g mL⁻¹ bubble (3–5 km, >15–17%). Note that data acquired for bubbles with bulk densities in the miscibility gap at T_{amb} and below 5 mW should never be used to calculate densities and by extension saturation pressures as it is very easy to either severely underestimate or overestimate the density of the bubble (see Figure 6A) when a single peak is fit to a spectrum composed of both liquid and vapor contributions (effectively reporting the density of either the liquid or vapor phase but not the bulk density). Our method to assess peak asymmetry can be used to help identify these spectra, even if the two peaks are not immediately obvious. We urge the reader not to use such data except to identify the presence of multiple phases in MI bubbles or fluid inclusions.

5 CONCLUSIONS AND RECOMMENDATIONS

We present the results of a series of experimental measurements on vapor bubbles from natural, olivine-hosted, CO₂-rich, melt inclusions from Mount Morning, Antarctica. Our measurements show that at T_{amb} , laser power has a strong effect on the Raman CO₂ spectrum. Distinct liquid and vapor peaks can be resolved at low laser powers (0.5, 1, 2, 5 mW) but

converge towards each other until they are indistinguishable at high laser powers (20 mW) regardless of the diffraction grating. Reports of natural MI vapor bubbles and fluid inclusions with densities in the miscibility gap at T_{amb} are likely due to a combination of laser heating effect due to laser power and lack of resolution to resolve both the liquid and vapor peaks. When both liquid and vapor peaks are fit, even at 12 mW, $\Delta\text{CO}_2\text{corr}$ measured corresponds to liquid and vapor at varying temperatures on our instrument.

Based on our findings we make the following recommendations:

- Researchers should systematically investigate the presence of liquid and vapor phases in the bubbles of their melt inclusions by microscopy (note that Brownian motion will not be visible when the bulb heats the sample above the critical temperature) and Raman spectroscopy at T_{amb} and low laser power (<2 mW). Researchers should not assume that the bubble or inclusion contents will be a single-phase when using <20 mW laser powers at sample. Significant density underestimations can occur.
- Any vapor bubble found to contain both liquid and vapor phases at T_{amb} or suspected to contain them (e.g. bubbles with bulk densities near that of liquid or vapor at T_{amb}) should preferably be analyzed while heating above T_{crit} , as close as possible to the calibration temperature, to minimize additional underestimation, and with as low laser power at sample as possible while still producing good signal/noise ratios.
- We echo the suggestion of [Hagiwara et al. \[2021\]](#), originally for high density fluid inclusions: users interested in analyzing bubbles of melt inclusions with bulk CO_2 densities in the miscibility gap by Raman spectroscopy should preferably do so while heating above T_{crit} and at a low laser power (<5 mW). This is because even when heating the sample above T_{crit} , using high laser powers can cause further heating and lead to an underestimation of the inclusion or bubble CO_2 density and resulting pressures and depths (e.g. 3–17% underestimation when using laser power at sample of 12–20 mW depending on the bulk density).
- When heating is impossible (i.e. all melt inclusions have already been exposed for further analyses and the vapor bubbles are lost), data acquired at T_{amb} with laser powers >12 mW on bubbles with bulk densities in the miscibility gap (especially above $>0.25 \text{ g mL}^{-1}$) may be sufficiently close to the bulk density of the bubble to provide at least a reasonable estimate (~10% pressure and depth underestimation based on the Cornell instrument “plateau”). In such cases, researchers should first establish whether a plateau is reached on their instrument to assess uncertainty. Further, raw spectra should be provided to assess asymmetry, acquisition conditions (laser power, integration times and accumulations) should be clearly reported, and the density should be considered minima.
- A simple Peltier module with center hole connected to a DC power supply is a simple and affordable solution to heat inclusions above the critical temperature and to monitor T during experiments.

AUTHOR CONTRIBUTIONS

CLD: Conceptualization, Methodology, Investigation, Validation, Formal Analysis, Writing – Original Draft, Writing – Review, Visualization.

KD: Investigation, Writing – Review.

EG: Conceptualization, Writing – Review, Resources – Instrumentation, Supervision, Funding Acquisition

AP: Conceptualization – Initial Research Question and Motivation, Resources – Samples, Writing – Review

GG: Conceptualization – Initial Research Question and Motivation, Writing – Review, Funding Acquisition.

PW: Software, Resources – Instrumentation, Investigation – Literature compilation, Writing – Review, Visualization, Funding Acquisition.

ACKNOWLEDGEMENTS

This project was supported by NSF EAR award No. EAR 1826673 to Gazel and Gaetani, NASA 20-SSW20-0066 to Gazel, and NSF award No. OPP 1644013 to Gaetani, and NSF award 2217371 and support from the Rose Hills Foundation through the Rose Hills Innovator Program at UC Berkeley to Wieser. We are grateful to Federica Schiavi and Jacob B. Lowenstern for their thorough and constructive reviews that helped significantly improve the manuscript. We also thank editor Jamie Farquharson for his constructive comments and fair handling of our manuscript.

DATA AVAILABILITY

Data acquired for this study are included in [Supplementary Material 1](#). Our peak asymmetry tool has been included as a module in python tool `DiadFit` v0.0.57 [<https://github.com/PennyWieser/DiadFit>; Wieser and DeVitre 2023] and an example notebook to calculate peak asymmetry is included in Supplementary Materials. The notebook is part of a series of examples included in the documentation for python tool `DiadFit` (<https://diadfit.readthedocs.io/en/latest/>).

COPYRIGHT NOTICE

© The Author(s) 2023. This article is distributed under the terms of the [Creative Commons Attribution 4.0 International License](#), which permits unrestricted use, distribution, and reproduction in any medium, provided you give appropriate credit to the original author(s) and the source, provide a link to the Creative Commons license, and indicate if changes were made.

REFERENCES

Allison, C. M., K. Roggensack, and A. B. Clarke (2019). “ $\text{H}_2\text{O}-\text{CO}_2$ solubility in alkali-rich mafic magmas: new experiments at mid-crustal pressures”. *Contributions to Mineralogy and Petrology* 174(7). doi: [10.1007/s00410-019-1592-4](https://doi.org/10.1007/s00410-019-1592-4).



Allison, C. M., K. Roggensack, and A. B. Clarke (2021). "Highly explosive basaltic eruptions driven by CO₂ exsolution". *Nature Communications* 12(1). doi: [10.1038/s41467-020-20354-2](https://doi.org/10.1038/s41467-020-20354-2).

– (2022). "MafiCH: a general model for H₂O–CO₂ solubility in mafic magmas". *Contributions to Mineralogy and Petrology* 177(3). doi: [10.1007/s00410-022-01903-y](https://doi.org/10.1007/s00410-022-01903-y).

Arakawa, M., J. Yamamoto, and H. Kagi (2008). "Micro-Raman thermometer for CO₂ fluids: Temperature and density dependence on Raman spectra of CO₂ fluids". *Chemistry Letters* 37(3), pages 280–281. doi: [10.1246/cl.2008.280](https://doi.org/10.1246/cl.2008.280).

Bali, E., M. E. Hartley, S. A. Halldórrsson, G. H. Gudfinnsson, and S. Jakobsson (2018). "Melt inclusion constraints on volatile systematics and degassing history of the 2014–2015 Holuhraun eruption, Iceland". *Contributions to Mineralogy and Petrology* 173(2). doi: [10.1007/s00410-017-1434-1](https://doi.org/10.1007/s00410-017-1434-1).

Berruex, L. G. and R. Freitag (2003). "Separation and purification of biochemicals". *Encyclopedia of Physical Science and Technology*. Elsevier, pages 651–673. doi: [10.1016/b0-12-227410-5/00683-9](https://doi.org/10.1016/b0-12-227410-5/00683-9).

Brown, M. S. and R. R. Steeper (1991). "CO₂-based thermometry of supercritical water oxidation". *Applied Spectroscopy* 45(10), pages 1733–1738. doi: [10.1366/000370291435319](https://doi.org/10.1366/000370291435319).

Buso, R., D. Laporte, F. Schiavi, N. Cluzel, and C. Fonquerne (2022). "High-pressure homogenization of olivine-hosted CO₂-rich melt inclusions in a piston cylinder: insight into the volatile content of primary mantle melts". *European Journal of Mineralogy* 34(3), pages 325–349. doi: [10.5194/ejm-34-325-2022](https://doi.org/10.5194/ejm-34-325-2022).

Dasgupta, R., M. M. Hirschmann, and N. D. Smith (2007). "Partial melting experiments of peridotite + CO₂ at 3 GPa and genesis of alkalic ocean island basalts". *Journal of Petrology* 48(11), pages 2093–2124. doi: [10.1093/petrology/egm053](https://doi.org/10.1093/petrology/egm053).

DeVitre, C. L., C. M. Allison, and E. Gazel (2021). "A high-precision CO₂ densimeter for Raman spectroscopy using a fluid density calibration apparatus". *Chemical Geology* 584, page 120522. doi: [10.1016/j.chemgeo.2021.120522](https://doi.org/10.1016/j.chemgeo.2021.120522).

Dixon, J. E. (1997). "Degassing of alkalic basalts". *American Mineralogist* 82(3-4), pages 368–378. doi: [10.2138/am-1997-3-415](https://doi.org/10.2138/am-1997-3-415).

Fall, A., B. Tattitch, and R. J. Bodnar (2011). "Combined microthermometric and Raman spectroscopic technique to determine the salinity of H₂O–CO₂–NaCl fluid inclusions based on clathrate melting". *Geochimica et Cosmochimica Acta* 75(4), pages 951–964. doi: [10.1016/j.gca.2010.11.021](https://doi.org/10.1016/j.gca.2010.11.021).

Ghiorso, M. S. and G. A. R. Gualda (2015). "An H₂O–CO₂ mixed fluid saturation model compatible with rhyolite-MELTS". *Contributions to Mineralogy and Petrology* 169(6). doi: [10.1007/s00410-015-1141-8](https://doi.org/10.1007/s00410-015-1141-8).

Gordon, H. R. and T. McCubbin (1966). "The 2.8-micron bands of CO₂". *Journal of Molecular Spectroscopy* 19(1-4), pages 137–154. doi: [10.1016/0022-2852\(66\)90237-2](https://doi.org/10.1016/0022-2852(66)90237-2).

Hagiwara, Y., K. Takahata, J. Torimoto, and J. Yamamoto (2018). "CO₂ Raman thermometer improvement: Comparing hot band and Stokes and anti-Stokes Raman scattering thermometers". *Journal of Raman Spectroscopy* 49(11), pages 1776–1781. doi: [10.1002/jrs.5461](https://doi.org/10.1002/jrs.5461).

Hagiwara, Y., K. Yoshida, A. Yoneda, J. Torimoto, and J. Yamamoto (2021). "Experimental variable effects on laser heating of inclusions during Raman spectroscopic analysis". *Chemical Geology* 559, page 119928. doi: [10.1016/j.chemgeo.2020.119928](https://doi.org/10.1016/j.chemgeo.2020.119928).

Hartley, M. E., J. MacLennan, M. Edmonds, and T. Thordarson (2014). "Reconstructing the deep CO₂ degassing behaviour of large basaltic fissure eruptions". *Earth and Planetary Science Letters* 393, pages 120–131. doi: [10.1016/j.epsl.2014.02.031](https://doi.org/10.1016/j.epsl.2014.02.031).

Iacono-Marziano, G., Y. Morizet, E. L. Trong, and F. Gaillard (2012). "New experimental data and semi-empirical parameterization of H₂O–CO₂ solubility in mafic melts". *Geochimica et Cosmochimica Acta* 97, pages 1–23. doi: [10.1016/j.gca.2012.08.035](https://doi.org/10.1016/j.gca.2012.08.035).

Iacovino, K., S. Matthews, P. E. Wieser, G. M. Moore, and F. Bégué (2021). "VESical part I: An open-source thermodynamic model engine for mixed volatile (H₂O–CO₂) solubility in silicate melts". *Earth and Space Science* 8(11). doi: [10.1029/2020ea001584](https://doi.org/10.1029/2020ea001584).

Kawakami, Y., J. Yamamoto, and H. Kagi (2003). "Micro-Raman densimeter for CO₂ inclusions in mantle-derived minerals". *Applied Spectroscopy* 57(11), pages 1333–1339. doi: [10.1366/000370203322554473](https://doi.org/10.1366/000370203322554473).

Lamadrid, H., L. Moore, D. Moncada, J. Rimstidt, R. Burruss, and R. Bodnar (2017). "Reassessment of the Raman CO₂ densimeter". *Chemical Geology* 450, pages 210–222. doi: [10.1016/j.chemgeo.2016.12.034](https://doi.org/10.1016/j.chemgeo.2016.12.034).

Lin, F., R. Bodnar, and S. Becker (2007). "Experimental determination of the Raman CH₄ symmetric stretching (v₁) band position from 1–650 bar and 0.3–22 °C: Application to fluid inclusion studies". *Geochimica et Cosmochimica Acta* 71(15), pages 3746–3756. doi: [10.1016/j.gca.2007.05.016](https://doi.org/10.1016/j.gca.2007.05.016).

Mironov, N., D. Tobelko, S. Smirnov, M. Portnyagin, and S. Krasheninnikov (2020). "Estimation of CO₂ content in the gas phase of melt inclusions using Raman spectroscopy: Case study of inclusions in olivine from the Karymsky Volcano (Kamchatka)". *Russian Geology and Geophysics* 61(5-6), pages 600–610. doi: [10.1537/rgg2019169](https://doi.org/10.1537/rgg2019169).

Moore, L. R., E. Gazel, R. Tuohy, A. S. Lloyd, R. Esposito, M. Steele-MacInnis, E. H. Hauri, P. J. Wallace, T. Plank, and R. J. Bodnar (2015). "Bubbles matter: An assessment of the contribution of vapor bubbles to melt inclusion volatile budgets". *American Mineralogist* 100(4), pages 806–823. doi: [10.2138/am-2015-5036](https://doi.org/10.2138/am-2015-5036).

Moore, L. R., N. Mironov, M. Portnyagin, E. Gazel, and R. J. Bodnar (2018). "Volatile contents of primitive bubble-bearing melt inclusions from Klyuchevskoy Volcano, Kamchatka: Comparison of volatile contents determined by mass-balance versus experimental homogenization". *Journal of Volcanology and Geothermal Research* 358, pages 124–131. doi: [10.1016/j.jvolgeores.2018.03.007](https://doi.org/10.1016/j.jvolgeores.2018.03.007).

Papale, P., R. Moretti, and D. Barbato (2006). "The compositional dependence of the saturation surface of H₂O + CO₂ fluids in silicate melts". *Chemical Geology* 229(1-3), pages 78–95. doi: [10.1016/j.chemgeo.2006.01.013](https://doi.org/10.1016/j.chemgeo.2006.01.013).

Robidoux, P., M. L. Frezzotti, E. H. Hauri, and A. Aiuppa (2018). “Shrinkage bubbles: The C–O–H–S magmatic fluid system at San Cristóbal Volcano”. *Journal of Petrology* 59(11), pages 2093–2122. doi: [10.1093/petrology/egy092](https://doi.org/10.1093/petrology/egy092).

Roedder, E. and R. J. Bodnar (1980). “Geologic pressure determinations from fluid inclusion studies”. *Annual Review of Earth and Planetary Sciences* 8(1), pages 263–301. doi: [10.1146/annurev.ea.08.050180.001403](https://doi.org/10.1146/annurev.ea.08.050180.001403).

Roedder, E. (1965). “Liquid CO₂ inclusions in olivine-bearing nodules and phenocrysts from Basalts”. *American Mineralogist* 50(10), pages 1746–1782. ISSN: 0003-004X.

– (1979). “Origin and significance of magmatic inclusions”. *Bulletin de Minéralogie* 102(5), pages 487–510. doi: [10.3406/bulmi.1979.7299](https://doi.org/10.3406/bulmi.1979.7299).

– (1984). *Fluid inclusions*. Volume 12. *Reviews in Mineralogy*. Mineralogical Society of America. ISBN: 0-939950-16-2.

Rosso, K. and R. Bodnar (1995). “Microthermometric and Raman spectroscopic detection limits of CO₂ in fluid inclusions and the Raman spectroscopic characterization of CO₂”. *Geochimica et Cosmochimica Acta* 59(19), pages 3961–3975. doi: [10.1016/0016-7037\(95\)94441-h](https://doi.org/10.1016/0016-7037(95)94441-h).

Song, Y., I. Chou, W. Hu, R. Burruss, and W. Lu (2009). “CO₂ density-Raman shift relation derived from synthetic inclusions in fused silica capillaries and its application”. *Acta Geologica Sinica* 83(5), pages 932–938.

Span, R. and W. Wagner (1996). “A new equation of state for carbon dioxide covering the fluid region from the triple-point temperature to 1100 K at pressures up to 800 MPa”. *Journal of Physical and Chemical Reference Data* 25(6), pages 1509–1596. doi: [10.1063/1.555991](https://doi.org/10.1063/1.555991).

Steele-MacInnis, M., R. Esposito, and R. J. Bodnar (2011). “Thermodynamic model for the effect of post-entrapment crystallization on the H₂O–CO₂ systematics of vapor-saturated, silicate melt inclusions”. *Journal of Petrology* 52(12), pages 2461–2482. doi: [10.1093/petrology/egr052](https://doi.org/10.1093/petrology/egr052).

Steele-MacInnis, M., R. Esposito, L. R. Moore, and M. E. Hartley (2017). “Heterogeneously entrapped, vapor-rich melt inclusions record pre-eruptive magmatic volatile contents”. *Contributions to Mineralogy and Petrology* 172(4). doi: [10.1007/s00410-017-1343-3](https://doi.org/10.1007/s00410-017-1343-3).

Sublett, D. M., E. Sendula, H. Lamadrid, M. Steele-MacInnis, G. Spiekermann, R. C. Burruss, and R. J. Bodnar (2020). “Shift in the Raman symmetric stretching band of N₂, CO₂, and CH₄ as a function of temperature, pressure, and density”. *Journal of Raman Spectroscopy* 51(3), pages 555–568. doi: [10.1002/jrs.5805](https://doi.org/10.1002/jrs.5805).

Taracsák, Z., M. Hartley, R. Burgess, M. Edmonds, F. Iddon, and M.-A. Longpré (2019). “High fluxes of deep volatiles from ocean island volcanoes: Insights from El Hierro, Canary Islands”. *Geochimica et Cosmochimica Acta* 258, pages 19–36. doi: [10.1016/j.gca.2019.05.020](https://doi.org/10.1016/j.gca.2019.05.020).

Thibault, Y. and J. R. Holloway (1994). “Solubility of CO₂ in a Ca-rich leucite: effects of pressure, temperature, and oxygen fugacity”. *Contributions to Mineralogy and Petrology* 116(1–2), pages 216–224. doi: [10.1007/bf00310701](https://doi.org/10.1007/bf00310701).

Tucker, J. M., E. H. Hauri, A. J. Pietruszka, M. O. Garcia, J. P. Marske, and F. A. Trusdell (2019). “A high carbon content of the Hawaiian mantle from olivine-hosted melt inclusions”. *Geochimica et Cosmochimica Acta* 254, pages 156–172. doi: [10.1016/j.gca.2019.04.001](https://doi.org/10.1016/j.gca.2019.04.001).

Venugopal, S., S. Moune, G. Williams-Jones, T. Druitt, N. Vigouroux, A. Wilson, and J. K. Russell (2020). “Two distinct mantle sources beneath the Garibaldi Volcanic Belt: Insight from olivine-hosted melt inclusions”. *Chemical Geology* 532, page 119346. doi: [10.1016/j.chemgeo.2019.119346](https://doi.org/10.1016/j.chemgeo.2019.119346).

Wallace, P. J., V. S. Kamenetsky, and P. Cervantes (2015). “Melt inclusion CO₂ contents, pressures of olivine crystallization, and the problem of shrinkage bubbles”. *American Mineralogist* 100(4), pages 787–794. doi: [10.2138/am-2015-5029](https://doi.org/10.2138/am-2015-5029).

Wang, W., M.-C. Caumon, A. Tarantola, J. Pironon, W. Lu, and Y. Huang (2019). “Raman spectroscopic densimeter for pure CO₂ and CO₂–H₂O–NaCl fluid systems over a wide P–T range up to 360 °C and 50 MPa”. *Chemical Geology* 528, page 119281. doi: [10.1016/j.chemgeo.2019.119281](https://doi.org/10.1016/j.chemgeo.2019.119281).

Wang, X., I.-M. Chou, W. Hu, R. C. Burruss, Q. Sun, and Y. Song (2011). “Raman spectroscopic measurements of CO₂ density: Experimental calibration with high-pressure optical cell (HPOC) and fused silica capillary capsule (FSCC) with application to fluid inclusion observations”. *Geochimica et Cosmochimica Acta* 75(14), pages 4080–4093. doi: [10.1016/j.gca.2011.04.028](https://doi.org/10.1016/j.gca.2011.04.028).

Wieser, P. E. and C. L. DeVitre (2023). “DiadFit: An Open-source Python3 tool for peak fitting of Raman data from silicate melts and CO₂ fluids”. *Earth ArXiv*. doi: [10.31223/x5cq1f](https://doi.org/10.31223/x5cq1f). [Preprint].

Wieser, P. E., K. Iacovino, S. Matthews, G. Moore, and C. M. Allison (2022). “VESical: 2. A critical approach to volatile solubility modeling using an open-Source Python3 engine”. *Earth and Space Science* 9(2). doi: [10.1029/2021ea001932](https://doi.org/10.1029/2021ea001932).

Wieser, P. E., H. Lamadrid, J. MacLennan, M. Edmonds, S. Matthews, K. Iacovino, F. E. Jenner, C. Gansecki, F. Trusdell, R. Lee, and E. Ilyinskaya (2021). “Reconstructing magma storage depths for the 2018 Kilauean eruption from melt inclusion CO₂ contents: The importance of vapor bubbles”. *Geochemistry, Geophysics, Geosystems* 22(2). doi: [10.1029/2020gc009364](https://doi.org/10.1029/2020gc009364).

Wojdyr, M. (2010). “Fityk: a general-purpose peak fitting program”. *Journal of Applied Crystallography* 43(5), pages 1126–1128. doi: [10.1107/s0021889810030499](https://doi.org/10.1107/s0021889810030499).

Yamamoto, J. and H. Kagi (2006). “Extended micro-Raman densimeter for CO₂ applicable to mantle-originated fluid inclusions”. *Chemistry Letters* 35(6), pages 610–611. doi: [10.1246/cl.2006.610](https://doi.org/10.1246/cl.2006.610).

Yuan, X. and R. A. Mayanovic (2017). “An empirical study on Raman peak fitting and its application to Raman quantitative research”. *Applied Spectroscopy* 71(10), pages 2325–2338.